AGU PUBLICATIONS

JGR

Journal of Geophysical Research: Planets

RESEARCH ARTICLE
10.1002/2014JE004617

Special Section:
Results from the first 360 Sols of the Mars Science Laboratory Mission: Bradbury Landing through Yellowknife Bay

Diagenetic origin of nodules in the Sheepbed member, Yellowknife Bay formation, Gale crater, Mars

K. M. Stack[1], J. P. Grotzinger[1], L. C. Kah[2], M. E. Schmidt[3], N. Mangold[4], K. S. Edgett[5], D. Y. Sumner[6], K. L. Siebach[1], M. Nachon[4], R. Lee[3], D. L. Blaney[7], L. P. Deflores[7], L. A. Edgar[8], A. G. Fairén[9], L. A. Leshin[10], S. Maurice[11], D. Z. Oehler[12], M. S. Rice[1], and R. C. Wiens[13]

[1]Department of Geological and Planetary Sciences, California Institute of Technology, Pasadena, California, USA, [2]Department of Earth and Planetary Sciences, University of Tennessee, Knoxville, Tennessee, USA, [3]Department of Earth Sciences, Brock University, St. Catharines, Ontario, Canada, [4]Laboratoire de Planétologie et Géodynamique de Nantes, Université de Nantes, Nantes, France, [5]Malin Space Science Systems, Inc., San Diego, California, USA, [6]Department of Earth and Planetary Sciences, University of California, Davis, California, USA, [7]Jet Propulsion Laboratory, California Institute of Technology, Pasadena, California, USA, [8]School of Earth and Space Exploration, Arizona State University, Tempe, Arizona, USA, [9]Department of Astronomy, Cornell University, Ithaca, New York, USA, [10]Department of Earth and Environmental Sciences and School of Science, Renssalaer Polytechnic Institute, Troy, New York, USA, [11]l'Institut de Recherche en Astrophyique et Planétologie de Toulouse, Université Paul Sabatier-Toulouse III, Toulouse, France, [12]Astromaterials Research and Exploration Science Directorate, NASA Johnson Space Center, Houston, Texas, USA, [13]Los Alamos National Laboratory, Los Alamos, New Mexico, USA

Key Points:
- Three types of nodules are observed in the Sheepbed mudstone
- Sheepbed nodules are interpreted as early diagenetic concretions
- Authigenic mineral precipitation was an important diagenetic process on Mars

Supporting Information:
- Readme
- Figure S1
- Text S1

Correspondence to:
K. M. Stack,
kstack@caltech.edu

Citation:
Stack, K. M., et al. (2014), Diagenetic origin of nodules in the Sheepbed member, Yellowknife Bay formation, Gale crater, Mars, *J. Geophys. Res. Planets*, *119*, 1637–1664, doi:10.1002/2014JE004617.

Received 28 JAN 2014
Accepted 18 JUN 2014
Accepted article online 21 JUN 2014
Published online 22 JUL 2014

Abstract The Sheepbed member of the Yellowknife Bay formation in Gale crater contains millimeter-scale nodules that represent an array of morphologies unlike those previously observed in sedimentary deposits on Mars. Three types of nodules have been identified in the Sheepbed member in order of decreasing abundance: solid nodules, hollow nodules, and filled nodules, a variant of hollow nodules whose voids have been filled with sulfate minerals. This study uses Mast Camera (Mastcam) and Mars Hand Lens Imager (MAHLI) images from the Mars Science Laboratory Curiosity rover to determine the size, shape, and spatial distribution of the Sheepbed nodules. The Alpha Particle X-Ray Spectrometer (APXS) and ChemCam instruments provide geochemical data to help interpret nodule origins. Based on their physical characteristics, spatial distribution, and composition, the nodules are interpreted as concretions formed during early diagenesis. Several hypotheses are considered for hollow nodule formation including origins as primary or secondary voids. The occurrence of concretions interpreted in the Sheepbed mudstone and in several other sedimentary sequences on Mars suggests that active groundwater systems play an important role in the diagenesis of Martian sedimentary rocks. When concretions are formed during early diagenetic cementation, as interpreted for the Sheepbed nodules, they have the potential to create a taphonomic window favorable for the preservation of Martian organics.

1. Introduction

The Mars Science Laboratory (MSL) Curiosity rover spent the first year of its mission in Gale crater exploring the record of a Hesperian-aged [*Grant et al.*, 2014] fluvio-lacustrine environment at Yellowknife Bay (Figure 1a) [*Grotzinger et al.*, 2014]. In this embayment of bedded, fractured rock, the rover team examined the Yellowknife Bay formation, a 5 m thick assemblage of siliciclastic sedimentary rocks of bulk basaltic composition (Figure 1b) [*Grotzinger et al.*, 2014]. The basal member of the Yellowknife Bay formation, the Sheepbed member, is a mudstone containing nearly 30% saponitic smectite clay [*Vaniman et al.*, 2014], suggesting a sustained interaction between Sheepbed sediments and surface or pore fluids with a circum-neutral pH [*McLennan et al.*, 2014]. The uniformly fine-grained nature of the Sheepbed member and the lateral preservation of thin beds (1–2 cm) indicate an origin via suspension settling in a low-energy, lacustrine setting [*Grotzinger et al.*, 2014]. Evidence for neutral water chemistry, variable redox states, and high water activity sustained at the surface of Mars for potentially thousands of years indicates that the Sheepbed mudstone records a habitable environment [*Grotzinger et al.*, 2014].

The Sheepbed member contains a variety of diagenetic textures that suggests a complex post-depositional aqueous history for this sedimentary rock [*Grotzinger et al.*, 2014; *McLennan et al.*, 2014; *Vaniman et al.*, 2014]. Within this set of textures, *Grotzinger et al.* [2014] documented the presence of nodules (cf. "solid nodules" of

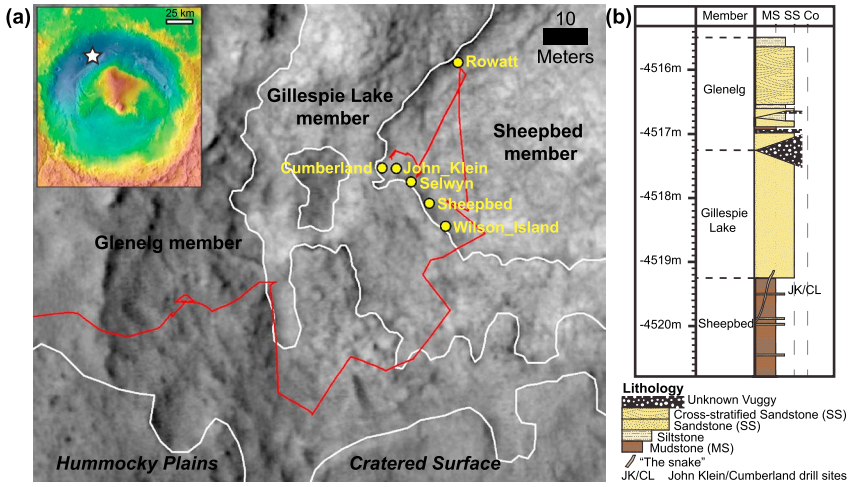

Figure 1. Adapted from *Grotzinger et al.* [2014] and *McLennan et al.* [2014]. (a) HiRISE image (PSP_010573_1755) of Yellowknife Bay showing the contacts between major geologic and geomorphic units, and the location of rover targets mentioned in the text. Red line represents the rover traverse up to sol 166. Inset shows the location of Yellowknife Bay in Gale crater on MOLA topography draped over a THEMIS Day IR mosaic. (b) Stratigraphic column of the Yellowknife Bay formation.

this paper), hollow nodules, and a variety of hollow nodules that are filled with sulfate minerals (cf. "filled nodules" of this paper) in the Sheepbed member (Figure 2). Mastcam images taken between sols 126 and 303 revealed that solid nodules are present throughout the entire 1.5 m interval of the Sheepbed member examined by the rover team,and likely occur along at least 50 m of exposed outcrop as defined by the Wilson_Island target to the south and the Rowatt target to the north (Figure 1a). Hollow nodules and filled nodules were first observed in the Sheepbed member at the Selwyn section and later in the vicinity of the John_Klein and Cumberland drill sites (Figure 1a). Solid, hollow, and filled nodules appear to be restricted to the Sheepbed member and have not been observed in the overlying Gillespie Lake or Glenelg members [*Grotzinger et al.,* 2014]. *Grotzinger et al.* [2014] interpreted all nodule types as diagenetic concretions and hypothesized that the hollow nodules formed when very early diagenetic fluids precipitated concretionary rims around gas bubbles trapped in the unlithified, uncompacted Sheepbed sediments. Filled nodules were interpreted as evidence for a later stage of diagenesis in which Ca-sulfate precipitated within the primary voids of some hollow nodules [*Grotzinger et al.*, 2014]. The presence of iron-bearing minerals (i.e., magnetite and akaganeite) in the Cumberland drill sample of a nodule-rich area of the Sheepbed outcrop led *Vaniman et al.* [2014] and *McLennan et al.* [2014] to propose a possible link between nodule formation and iron-bearing compounds.

This study builds on the work of *Grotzinger et al.* [2014] and *McLennan et al.* [2014] by presenting a quantitative analysis of the size, shape, and spatial distribution of Sheepbed member nodules. These observations are used to test potential nodule origins, and will be used to show that a diagenetic concretionary origin is the most parsimonious explanation for the Sheepbed nodules. Nodule size and shape measured with Mars Hand Lens Imager (MAHLI) images are used to understand petrophysical and compositional properties of the Sheepbed sediments and the relative timing of nodule formation. Lateral and vertical distributions of nodules measured in Mastcam mosaics provide insight into fluid availability and cm-scale heterogeneities in the Sheepbed sediments at the time of nodule formation, as well as the relationship between nodules and other diagenetic features observed in the Sheepbed mudstone. Geochemical data from the Alpha Particle X-Ray Spectrometer (APXS) and ChemCam Laser Induced Breakdown Spectrometer (LIBS) provide additional constraints on models for nodule growth. Understanding the origin and distribution of nodules in the Sheepbed member is essential for assessing the aqueous history of the Yellowknife Bay formation, the potential habitability of Gale crater, and the significance of aqueous diagenesis in the Martian sedimentary rock record.

2. Data and Methods

2.1. Nodule Classification and Nomenclature

Nodules were defined by *Grotzinger et al.* [2014] as "millimeter-scale protrusions of the outcrop with 3D differential relief suggesting crudely spherical geometries," while hollow nodules were defined as

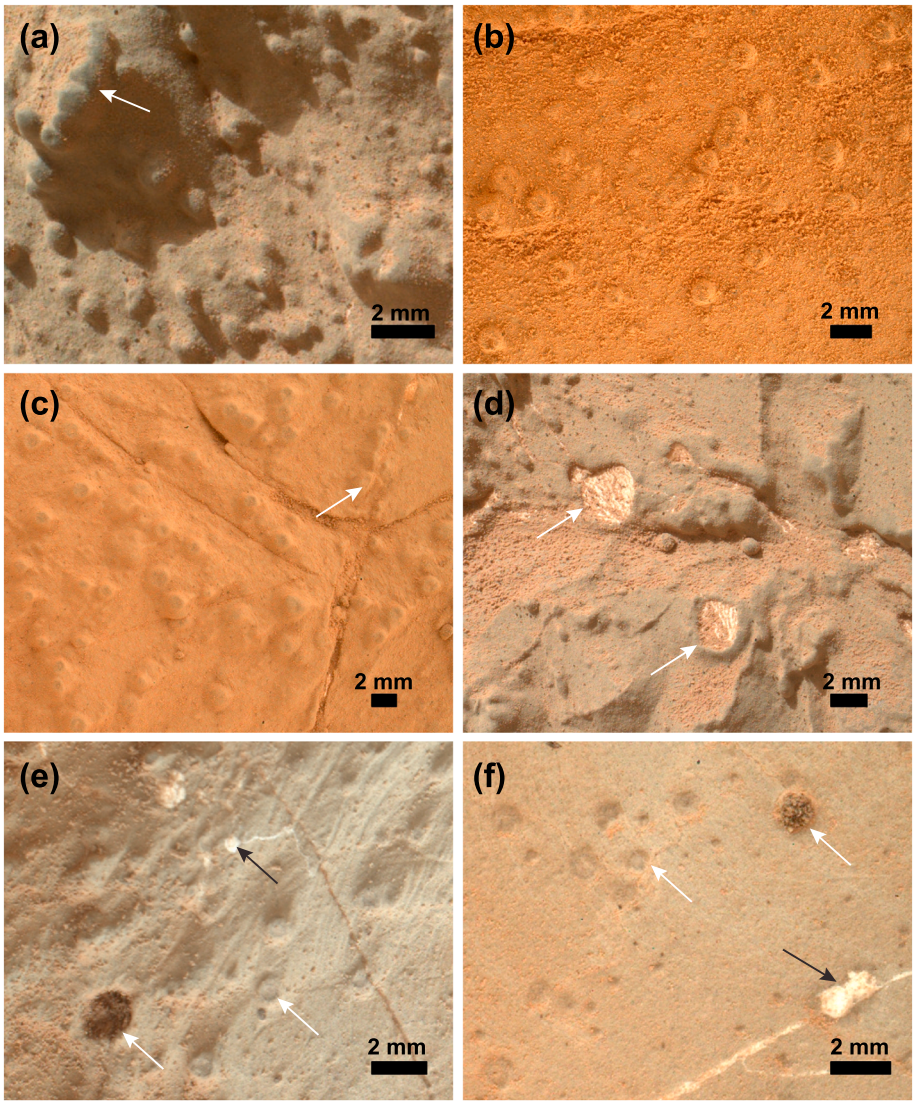

Figure 2. MAHLI images of solid, hollow, and filled nodules. (a) MAHLI image 0154MH0001710000101524R00 of target Persillon taken on sol 154. This area contains abundant solid nodules. The white arrow points toward a sextuplet of six concatenated solid nodules. (b) MAHLI image 0169MH0001630000102238R00 of target Brock_Inlier taken on sol 169 showing "dimpled" hollow nodule morphology. (c) MAHLI image 0275MH0002580000102991R00 of dimpled hollow nodules of the Cumberland target taken on sol 275. White arrow points to a sulfate-filled fracture that crosscuts dimpled hollow nodules. (d) MAHLI image 0154MH0001710000101524R00 of target Persillon showing filled nodules. Filled nodules are interpreted as hollow nodules filled with sulfate minerals during a later phase of diagenesis. (e) MAHLI image 0291MH0002770010103392C00 of brushed target Cumberland_DRT taken on sol 291 showing dimpled and bowl-like hollow nodule voids (white arrows) and a sulfate-filled bleb (black arrow) connected by hairline fractures. (f) MAHLI image 0173MH0002270000102314R00 of brushed target Wernecke_3 showing dimpled and bowl-like hollow nodules (white arrows) and a filled nodule doublet (black arrow) associated with sulfate-filled hairline cracks.

"millimeter-scale circular rims with hollow centers." Filled hollow nodules were described by *Grotzinger et al.* [2014] as circular rims surrounding an interior of sulfate and were interpreted as hollow nodules that had been filled by Ca-sulfate during a later phase of diagenesis.

This study also recognizes three types of nodules but employs a slightly modified version of *Grotzinger et al.*'s [2014] nomenclature to describe the nodule types observed in the Sheepbed member. In this study, the term "nodule" is used in a generic way to refer to all features in the Sheepbed that are millimeter-scale, generally spheroidal protrusions from the outcrop. Nodules that exhibit no discernable interior structure and are defined exclusively by external shape, size, and relief are referred to as solid nodules (Figure 2a). Solid nodules

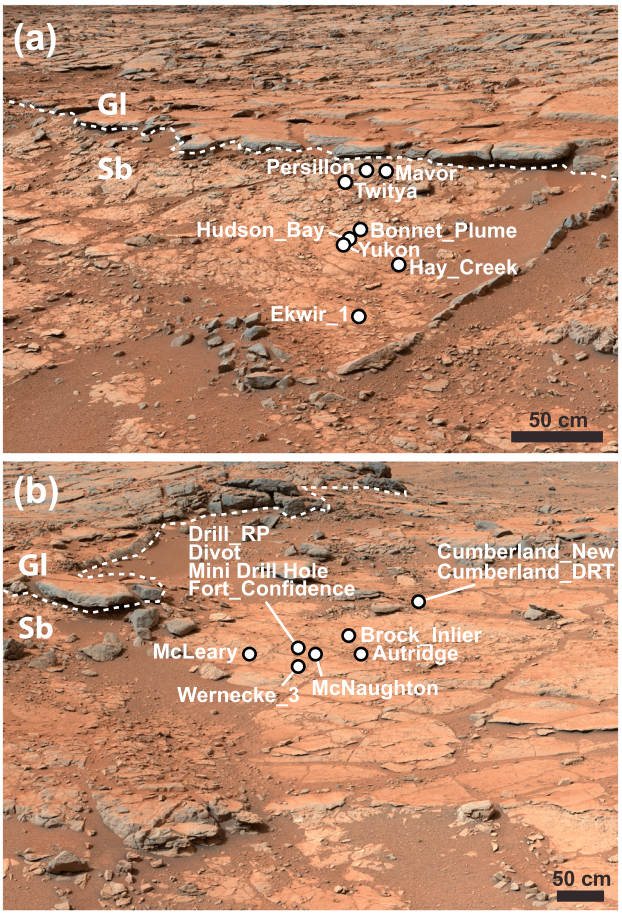

Figure 3. MAHLI targets from the (a) Selwyn section plotted on an M-100 Mastcam mosaic acquired on sol 137. (b) John Klein and Cumberland drill locations plotted on an M-100 Mastcam mosaic acquired on sol 138. Dashed white lines indicate the contact between the Sheepbed and Gillespie Lake members.

described herein are equivalent to *Grotzinger et al.*'s [2014] "nodules." Nodules that exhibit internal structure are classified here as either hollow nodules or filled nodules. As in *Grotzinger et al.* [2014], hollow nodules are nodules whose interiors are exposed showing a central void surrounded by a circular raised rim (Figures 2b and 2c). Filled nodules are defined here as nodules containing two distinct phases within their interiors: a circular raised rim similar in appearance to the host rock and a sulfate mineral-filled interior (Figures 2d–2f), and are equivalent to *Grotzinger et al.*'s [2014] sulfate-filled hollow nodules.

2.2. MAHLI

MAHLI is a 2 megapixel camera mounted on the Curiosity rover arm capable of imaging subjects at working distances between 2.1 cm and infinity at a maximum resolution of ~14 μm [*Edgett et al.*, 2012]. The sizes of individual solid, hollow, and filled nodules were measured in 20 MAHLI images obtained between sols 150 and 291 (Figure 3 and Table 1). The MAHLI images used in this study were acquired at working distances between 2.8 and 11.2 cm, resulting in image resolutions ranging from 16.7 to 46.3 μm/pixel (Table 1). Of the 20 MAHLI images used in this study, half were planned by the MSL science team with the express purpose of targeting nodule-bearing portions of the Sheepbed outcrop. The other 10 images were acquired for other purposes but happen to contain nodules. For each MAHLI image, nodules in the imaged scene were first identified and classified as solid, hollow, or filled. Then, the two-dimensional outline of each nodule was traced manually using ArcGIS software (Figure S1 in the supporting information). Individual traces were converted to circles using the minimum bounding geometry algorithm in ArcGIS to obtain a diameter for each feature. These data were used to calculate size statistics, make histograms, and compare rim thickness and interior void diameter of hollow nodules (Figures 4 and 5 and Table 2). Diameters were also used to estimate areal concentration, C, of each nodule type within the outcrop covered by each MAHLI image using the formula of *McLennan et al.* [2005]:

$$C = \pi n d^2 / 6A \quad (1)$$

where n is the number of features on an assumed planar rock surface with area A and d is the mean diameter of these features (Table 1).

Calculating nodule diameter using the minimum bounding geometry assumes that each nodule is spherical and thus yields circular cross sections. To test this assumption, diameter traces were also fit to a rectangle by width using the minimum bounding geometry in ArcGIS. This algorithm provided two perpendicular axes for each rectangular fit and permitted calculation of an aspect ratio (AR) for each nodule (Table 2). Nodule shapes were classified according to *Blatt et al.* [1972] and *McBride et al.* [1999], who describe features with aspect ratios less than 1.5:1 as equant or circular, while those with aspects greater than 2.5:1 are elongate. Those of intermediate aspect between 1.5:1 and 2.5:1 are considered subequant or subcircular.

AGU Journal of Geophysical Research: Planets 10.1002/2014JE004617

Table 1. MAHLI Images Used to Measure the Size, Shape, and Concentration of Solid, Hollow, and Filled Nodules

Target	Sol	Image ID	Product Type	Working Distance (cm)	Pixel Scale (μm/pixel)	$n_{solid\ nodules}$	$C_{solid\ nodules}$ (%)	$n_{hollow\ nodules}$	$C_{hollow\ nodules}$ (%)	$n_{filled\ nodules}$	$C_{filled\ nodules}$ (%)
Ekwir_1	150	0150MH0001630000101432R00	onboard focus merge	6.7	30.4	11	0.2	47	2.0	2	0.3
Persillon	154	0154MH0001710000101524R00	onboard focus merge	7.0	31.5	277	4.3	24	2.0	5	2.2
Mavor	158	0158MH0001850000101699R00	onboard focus merge	7.1	32.5	100	1.3	13	0.5	-	-
Twitya	159	0159MH0000900000101730R00	onboard focus merge	6.7	30.4	42	0.9	8	2.2	-	-
Yukon	161	0161MH0001630000101918R00	onboard focus merge	6.9	31.2	49	2.8	-	-	-	-
Bonnet_Plume_1	161	0161MH0001920000101908R00	onboard focus merge	6.8	30.8	235	1.8	20	0.4	-	-
Bonnet_Plume_2	161	0161MH0001920000101910R00	onboard focus merge	2.8	16.7	49	1.4	2	0.4	-	-
Hudson_Bay	161	0161MH0001630000101922R00	onboard focus merge	4.1	21.4	84	1.6	6	0.5	-	-
Hay_Creek	162	0162MH0001930000101964R00	onboard focus merge	6.9	31.1	49	2.7	16	1.3	1	0.4
Drill_RP	168	0168MH0001630000102166R00	onboard focus merge	6.7	30.2	36	1.2	27	2.3	6	2.2
Brock_Inlier	169	0169MH0001630000102240R00	onboard focus merge	6.9	31.0	73	2.0	34	2.0	1	0.1
Autridge	173	0173MH0002270000102318R00	onboard focus merge	4.7	23.4	35	1.3	3	0.2	2	0.1
Wernecke_3	173	0173MH0002270000102314R00	onboard focus merge	6.2	28.6	135	1.0	50	1.6	2	0.3
Divot	174	0174MH0001460010102325E01	full-frame based on autofocus subframe	10.8	45.0	209	2.8	34	1.0	-	-
Mini Drill Hole	178	0178MH0002110000102475R00	onboard focus merge	6.5	29.5	33	1.3	21	1.3	4	1.1
Fort_Confidence	179	0179MH0002020000102510R00	onboard focus merge	4.1	21.2	24	2.0	3	0.5	1	0.4
McNaughton	181	0181MH0001630000102614R00	onboard focus merge	6.6	30.0	102	2.4	29	1.6	5	0.4
McLeary	181	0181MH0001630000102620R00	onboard focus merge	6.4	29.2	35	1.4	21	1.3	-	-
Cumberland_New	275	0275MH0002580000102991R00	onboard focus merge	11.2	46.3	100	2.5	81	2.5	-	-
Cumberland_DRT	291	0291MH0002770010103392C00	full-frame based on autofocus subframe	7.0	31.7	51	1.3	74	3.1	1	0.1

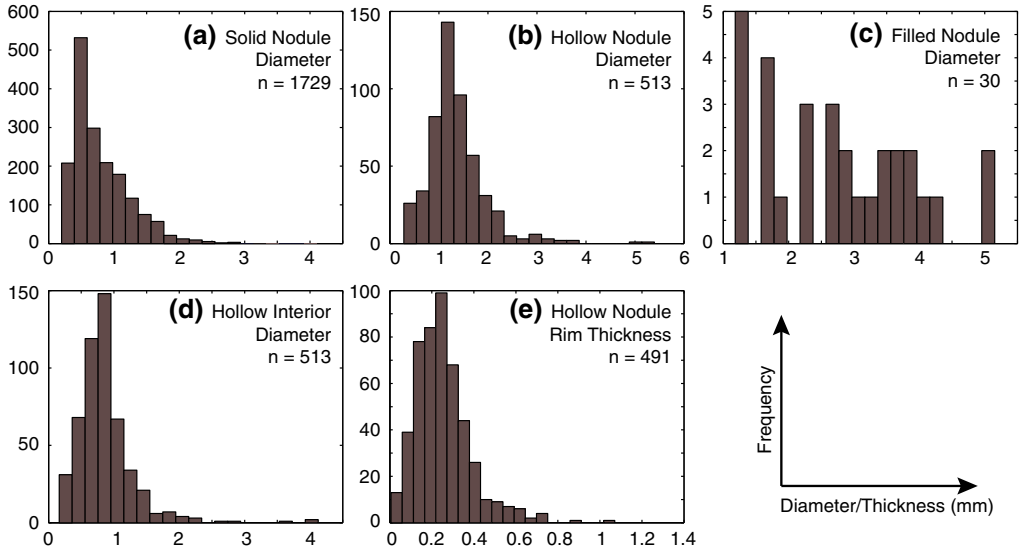

Figure 4. Size frequency histograms of (a) solid nodule diameter, (b) hollow nodule diameter, (c) filled nodule diameter, (d) hollow nodule interior void diameter, and (e) hollow nodule rim thickness.

Wilcoxon rank sum testing in Matlab was used to determine whether the size and shape of one type of nodule is statistically similar or distinct from the other nodule types. The Wilcoxon rank sum test tests the null hypotheses that the diameters and aspect ratios of two nodule types are sampled from continuous distributions with equal medians (Table 3). This test assumes that the two samples are independent but does not require the samples to follow a normal distribution because it tests for equal medians, not means. The null hypothesis is rejected at a 5% significance level (significance probability, p, < 0.05).

2.3. Mastcam

Images of the Sheepbed outcrop taken with the focusable M-100 (100 mm fixed focal length) camera mounted on the rover mast were mosaicked to facilitate mapping of the lateral and vertical distributions of nodule types (Figure 6). The four mosaics (John Klein, Cumberland 1, Cumberland 2, and Raised Ridges and Nodules) used in this study to map the lateral distribution of nodules (i.e., within the same stratigraphic level) were acquired in the nearfield workspace area of the rover and cover relatively flat, wind-exposed outcrop surfaces of the Sheepbed mudstone (Figures 7–10). Because the M-100 camera was pointed nearly downward during image acquisition, mosaics were projected to a viewing geometry normal to the outcrop surface so that the mosaic resolution, 0.1 mm/pixel, was constant across the mosaic. These projections resulted in minimal feature distortion and permitted quantification of nodule distribution.

For each of the four mosaics, nodules were manually tabulated by point counting in ArcGIS software after the mosaics were enhanced in contrast and brightness to enable feature identification. Since much of the Sheepbed member is thinly, but variably, coated with dust, distinguishing hollow nodules from filled nodules was sometimes difficult at the mosaic resolution (0.1 mm/pixel). Distinguishing hollow/filled nodules from solid nodules was also challenging when hollow and filled nodule interior diameters approached the mosaic resolution. As a result, hollow and filled nodules were point counted together and are likely underrepresented relative to solid nodules. The point counts of solid and hollow/filled nodules were then used to create concentration maps in ArcGIS (Figures 7–10) and to calculate average nearest neighbor statistics using the ArcGIS Spatial Statistics Toolbox (Table 4). The Average Nearest Neighbor tool measures the average distance between a feature and its nearest neighbor and compares this value with the expected average distance for features that are randomly distributed. If the ratio of measured distance to expected distance is less than one, the features exhibit

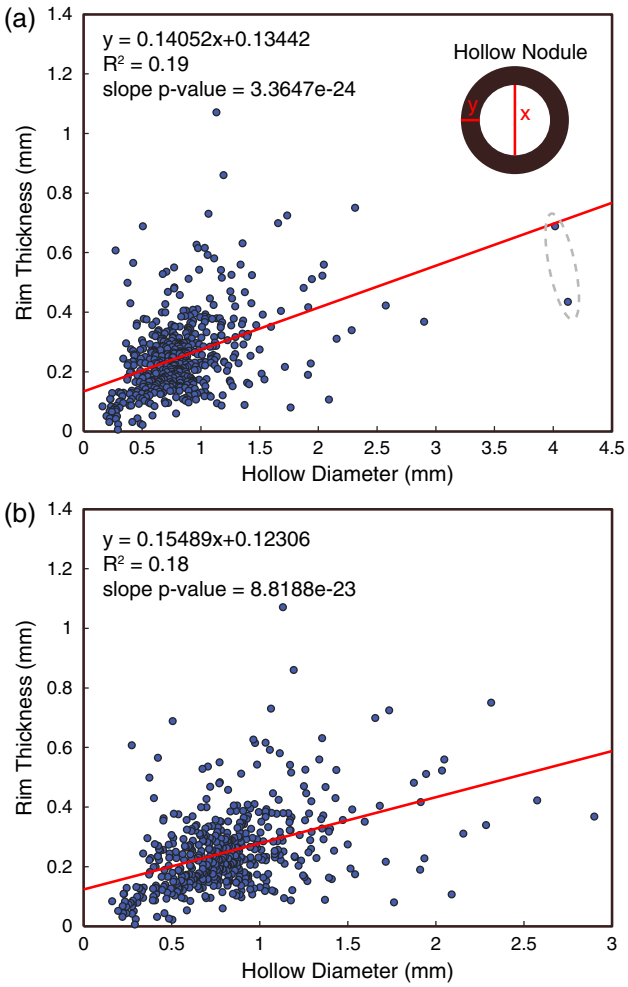

Figure 5. Plots of hollow nodule rim thickness versus hollow nodule interior void diameter. (a) Linear regression model of 491 rims and corresponding hollow void interiors measured in MAHLI images, two potential outliers circled in gray. (b) Linear model and scatter plot for data set excluding the two potential outliers identified in Figure 5a. For both data sets, slope *p*-values $<<0.05$ indicating that the null hypothesis that the slope is zero is rejected.

clustering. If the ratio is greater than one, the features are dispersed. The null hypothesis that the features are distributed randomly is rejected at a 5% significance level.

The vertical distribution of solid and hollow/filled nodules (i.e., across stratigraphic intervals) within the Sheepbed member was also examined in two spherically projected mosaics (Selwyn and Yellowknife Bay Egress) produced by Malin Space Science Systems, both targeted near an area of the Sheepbed informally named the Selwyn section (Figures 6, 12, and 13). These mosaics could not be vertically projected or georectified without significant distortion or loss of image resolution, so the pixel scale of these mosaics differs throughout the image scene. As a result, nodule distributions illustrated in these mosaics are qualitative, rather than quantitative, and nearest neighbor statistics were not calculated.

2.4. APXS

APXS elemental data were acquired for 17 individual rock targets spanning 1.5 m of the Sheepbed member stratigraphic section over Sols 129 to 271. All analyses were conducted on nonbrushed rock surfaces, which were variably coated by fine dust. Two of these targets (including Wernecke) were also analyzed after brushing with the Dust Removal Tool (DRT) [*Anderson et al.*, 2012]. Six APXS targets have nodules visible within the APXS field of view (FOV) in corresponding MAHLI images (Figures 14a and 14b). For these six targets, elemental ratios were plotted against nodule abundance within the APXS FOV to help identify trends indicative of nodule composition (Figures 14a and 14b). To quantify the nodule abundance in the APXS field of view, MAHLI image contrast was enhanced with Adobe Photoshop, and ImageJ was used to find the fraction of the area containing visible nodules.

Table 2. Nodule Size and Shape Statistics

	Diameter (*d*)						Aspect Ratio (*AR*)				
	n	μ_d (mm)	σ_d (mm)	Median *d* (mm)	Min *d* (mm)	Max *d* (mm)	μ_{AR}	σ_{AR}	Median *AR*	Min *AR*	Ma × *AR*
Solid Nodules	1729	0.80	0.44	0.66	0.20	4.11	1.23	0.21	1.17	1.00	3.27
Hollow Nodules (Whole)	513	1.35	0.59	1.27	0.29	5.40	1.17	0.13	1.13	1.01	1.93
Hollow Nodule Interior Voids	513	0.86	0.44	0.81	0.16	4.13	1.24	0.22	1.19	1.00	3.41
Hollow Nodule Rim Thickness	491	0.25	0.14	0.23	0.01	1.07	—	—	—	—	—
Filled Nodules	30	2.75	1.14	2.72	1.18	5.15	1.16	0.17	1.12	1.01	1.97

Table 3. Wilcoxon Rank Sum Test Results

Data Sets Tested	Parameter	*p*	Null Hypothesis Rejected?
Solid nodule versus hollow nodule	*d*	8.00E−96	Yes
Solid nodule versus filled nodule	*d*	1.28E−18	Yes
Hollow nodule versus filled nodule	*d*	5.49E−12	Yes
Solid nodule versus hollow nodule	*AR*	8.55E−09	Yes
Solid nodule versus filled nodule	*AR*	0.0469	Yes
Hollow nodule versus filled nodule	*AR*	0.3795	No

2.5. ChemCam

ChemCam [*Wiens et al.*, 2012, 2013] was also used to assess compositional differences between the nodules and host Sheepbed mudstone. Two types of observations were made with ChemCam. The first strategy involved a comparison between the average composition of the Sheepbed member and the composition of areas enriched in nodules (Table 5). In this case, the 30 shots fired at each LIBS location have the potential to record a difference in composition related to the presence of nodules. A total of 128 ChemCam LIBS shot sites in areas with a high concentration of nodules were selected: DT-RP5 (sol 166), Kazan (sol 187, 274), Cumberland (sol 187, 274, 275), Rae (sol 189, sol 192), Ruth (sol 232), and Duluth (sol 292). These observations were compared to 354 other shot sites that visually appear to have analyzed pure mudstone. Quantification of ChemCam data utilized a partial least square (PLS) method corresponding to a comparison of multiple emission lines of each major element with a laboratory database performed on Earth [see, e.g., *Wiens et al.,* 2013]. A second ChemCam strategy utilized depth profiles that correspond to an intense burst of 150 to 600 shots laser shots at a single location. Whereas 30 shots can penetrate several tens of micrometers in the softest rocks, 150 shots likely penetrates >100 μm [*Wiens et al.*, 2012]. The ChemCam observation DT-RP5 (sol 166) consisted of four locations with 150 shots each in a nodule-rich area near the John Klein drill hole (Figure 15).

3. Shape and Size Distributions

3.1. Solid Nodules

A total of 1729 solid nodules embedded in the outcrop were identified and measured in 20 MAHLI images of the Sheepbed member. Mean solid nodule diameter is 0.80 mm, with a minimum measured diameter of 0.20 mm and a maximum diameter of 4.11 mm (Table 2). The size-frequency distribution of solid nodule diameters is positively skewed around a mode of 0.5 mm (Figure 4a). For diameters larger than this mode, frequency decreases as solid nodule diameter increases, following a lognormal distribution. The areal concentration of solid nodules varies from target to target, ranging from 0.2% at Ekwir_1 to 4.3% at Persillon (Table 1). The overall areal concentration of solid nodules is 1.8%, obtained by averaging all 20 MAHLI target densities.

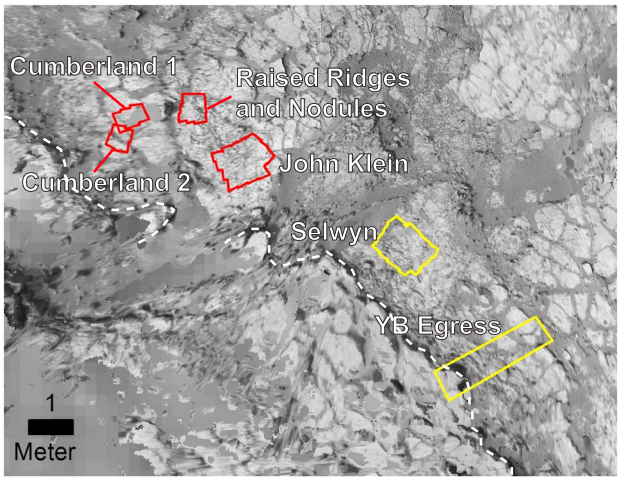

Figure 6. Navigation camera (Navcam) overhead projection showing image footprints of the four Mastcam mosaics used to map lateral distributions of solid and hollow/filled nodules (red), and the two Mastcam mosaics used to map vertical distributions of solid and hollow/filled nodules (yellow). Dashed white line indicates the Sheepbed-Gillespie Lake contact.

Solid nodules are generally circular in cross section, with an average measured aspect ratio of 1.2 (Table 2). Of the 1729 solid nodules measured, 1574 (91%) are circular ($AR < 1.5{:}1$), 153 (9%) are subcircular circular ($1.5{:}1 > AR < 2.5{:}1$), and only 2 (0.1%) are elongate ($AR > 2.5{:}1$). Solid nodules are generally circular or subcircular whether exposed on horizontal (i.e., Wernecke_3, Figure 2f) or vertical (i.e., Persillon, Figure 2a) exposures and appear to exhibit spherical

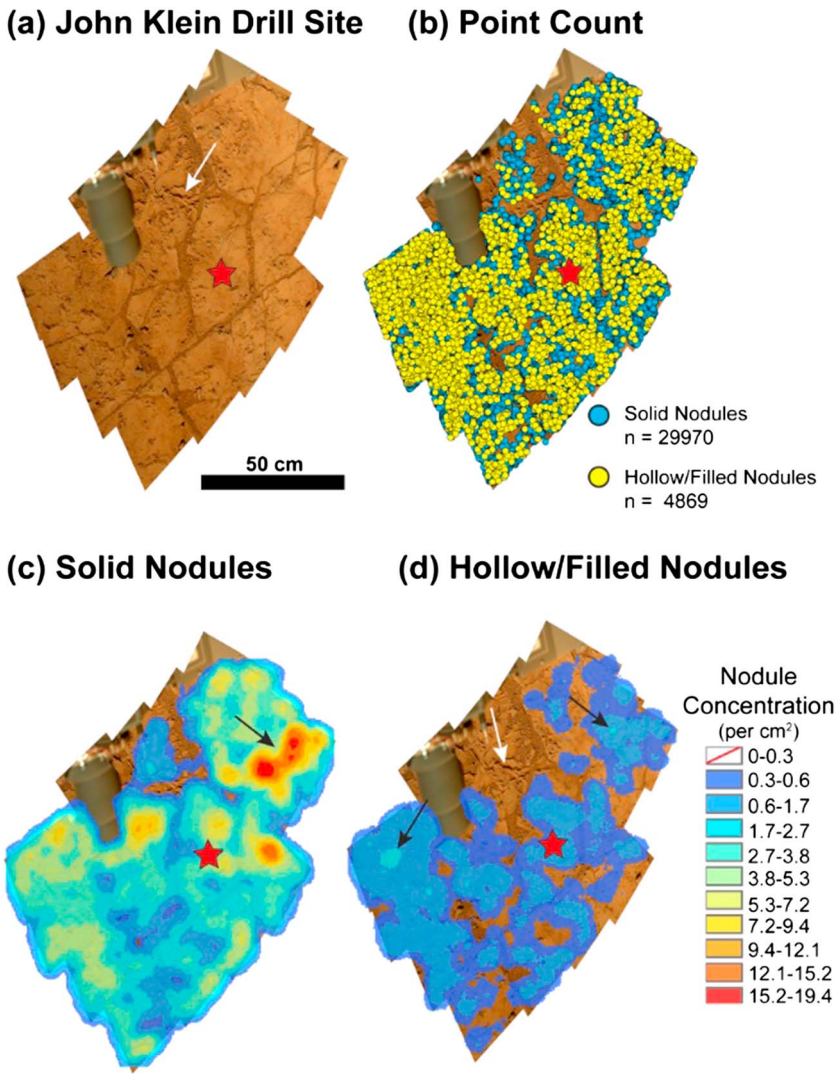

Figure 7. Solid and hollow/filled nodules mapped in the vicinity of the John_Klein drill site (red star) in an M-100 mosaic taken on sol 166. See supporting information for a list of image IDs. (a) John Klein mosaic. The red star represents the location of the John_Klein drill hole; the white arrow points to a dense network of raised ridges. (b) Point count of solid nodules and hollow/filled nodules. (c) Map showing the distribution and concentration of solid nodules. Black arrow points to the area of highest solid nodule concentration. (d) Map showing the distribution and concentration of hollow/filled nodules. White arrow highlights the area around the raised ridge network where hollow/filled nodules are largely absent. Black arrows point to regions of relatively high hollow/filled nodule concentration.

rather than prolate or oblate spheroidal shapes. Solid nodules do not exhibit any internal lamination and are not observed to contain through-going laminae. In the few intervals where intercalated beds do occur within the Sheepbed, solid nodules do not appear to influence or be influenced by bedding. Individual solid nodules are generally isolated within the matrix, but in some areas of particularly high nodule concentration (e.g., Persillon), agglutinated solid nodules (twins, triplets, and even sextuplets) are not uncommon (Figure 2a).

3.2. Hollow Nodules

Five hundred thirteen hollow nodules were identified in the MAHLI image set (Table 1). Although hollow nodules are generically defined as protrusions whose interiors are exposed showing a central void surrounded by a circular raised rim, a range of hollow nodule morphologies were observed in the MAHLI images. Some hollow nodules were characterized by prominent, positive relief rims and subtle interior voids that appeared as dimples or slight impression in the center of the nodule (Figures 2b and 2c), while other hollow nodules are characterized by empty bowl-like voids and more subtle positive relief rims (Figures 2e

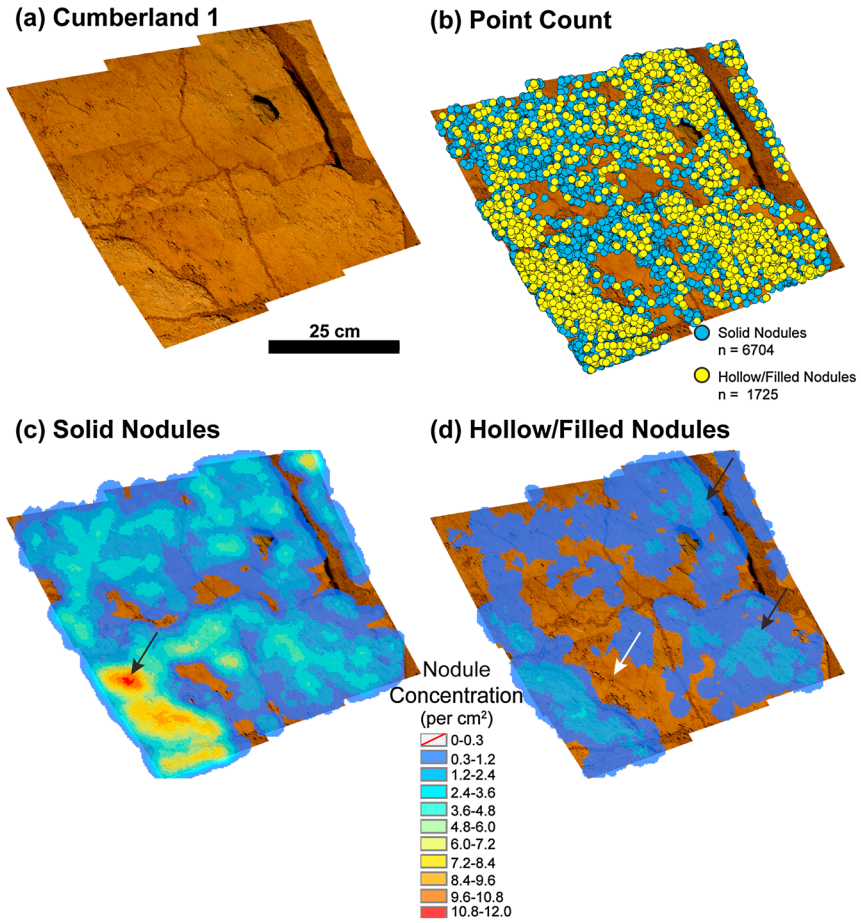

Figure 8. Cumberland 1 M-100 mosaic taken on sol 185 showing solid and hollow/filled nodules in the vicinity of the Cumberland drill hole. See supporting information for a list of image IDs. (a) Cumberland 1 mosaic. (b) Point count of solid nodules and hollow/filled nodules. (c) Map showing the distribution and concentration of solid nodules. Black arrow points to the area of highest solid nodule concentration. (d) Map showing the distribution and concentration of hollow/filled nodules. White arrow points to an area largely devoid of hollow/filled nodules. Black arrows point to relatively intermediate to high concentrations of hollow/filled nodules along the edge of the outcrop block.

and 2f). Still other hollow nodules exhibit morphologies intermediate between bowl and dimple-like voids. A variety of hollow nodule morphologies coexist within the individual MAHLI image scenes and do not appear to be spatial segregated in a systematic way. As such, combined size and shape measurements for all hollow nodules morphologies are reported below.

The mean hollow nodule diameter is 1.35 mm (Table 2), and diameters range from 0.29 mm to 5.40 mm. A histogram of diameter frequency (Figure 4b) shows a nearly Gaussian distribution between 0 and 2.5 mm centered on a mode just greater than 1 mm, but the infrequent occurrence of hollow nodules greater than 2.5 mm gives the distribution a positive skew. The areal concentration of hollow nodules varies from target to target (Table 1): Autridge has the lowest concentration of hollow nodules at 0.2%, while Cumberland_DRT has the highest concentration at 3.1%. Average areal concentrations for all MAHLI target images containing hollow nodules (excludes Yukon) is 1.4%. The average aspect ratio measured for hollow nodules is 1.17 (Table 2), suggesting that these features are generally circular in cross section. Of the 513 hollow nodules measured, 501 (98%) are circular ($AR < 1.5{:}1$) while 12 (2%) are subcircular ($1.5{:}1 < \mathrm{AR} > 2.5{:}1$). None are considered elongate.

The average diameter of preserved void space within the hollow nodules is 0.86 mm ($n = 513$) (Table 2), ranging from 0.16 mm to 4.13 mm. As with external diameters, preserved voids show a nearly Gaussian distribution (Figure 4d) between 0 and 1.5 mm, centered around a mode just less than 1 mm. The low frequency occurrence of hollow nodule interiors greater than 2 mm gives the distribution a positive skew. The average aspect ratio

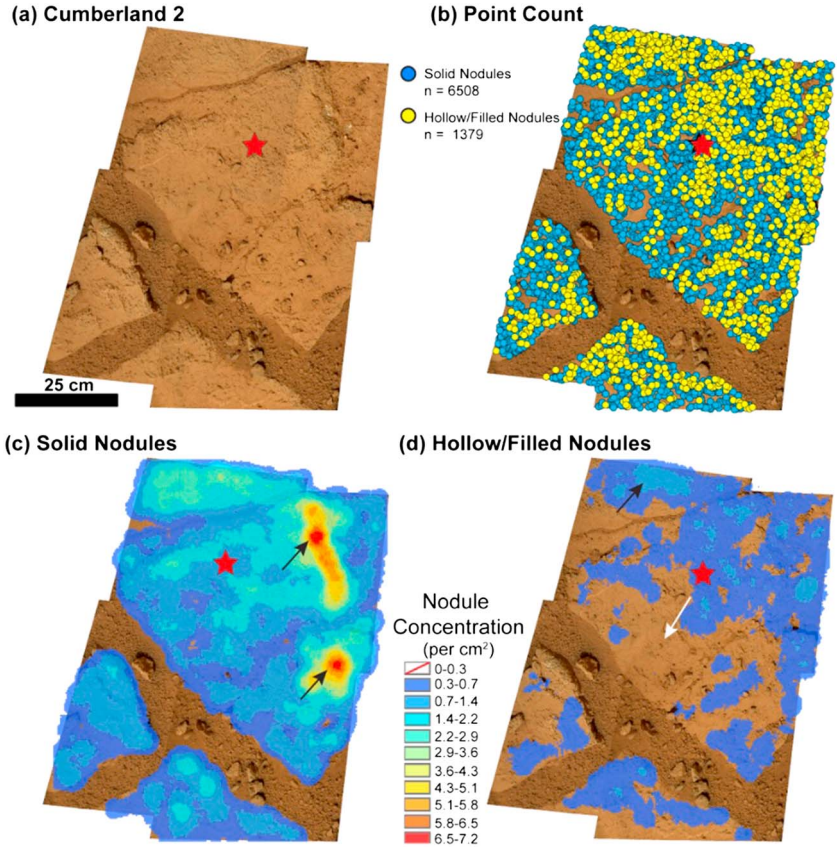

Figure 9. Cumberland 2 mosaic showing solid nodules and hollow/filled nodules in the vicinity of the Cumberland drill hole (red star) in an M-100 mosaic taken on sol 275. See supporting information for a list of image IDs. (a) Cumberland 2 mosaic. (b) Point count of solid and hollow/filled nodules. (c) Map showing the distribution and concentration of solid nodules. Black arrows point to areas of highest solid nodule concentration. (d) Map showing the distribution and concentration of hollow/filled nodules. White arrow points to a portion of the outcrop devoid of hollow/filled nodules. Black arrow points to region of highest hollow/filled nodule concentration.

measured for hollow nodule interiors is 1.24 (Table 2), suggesting that interior voids are generally circular in cross section. Of the 513 hollow nodule interiors measured, 471 (92%) are circular ($AR < 1.5$:1), 39 (8%) are subcircular (1.5:1 $< AR >$ 2.5:1), and 3 interiors (.6%) are considered elongate ($AR > 2.5$:1).

Rim thickness was calculated for each hollow nodule by determining the difference between external and interior diameters, then dividing by two. This method assumes a circular cross section and that the interior hollow is perfectly centered within the nodule. This is clearly not the case for every hollow nodule, but this calculation provides a reasonable estimate for hollow nodule rim thickness. In the Ekwir_1 target image (Figure A1 in the supporting information), not all nodules identified as hollow nodules have rims as a result of erosion and abrasion of the rock surface by the DRT brush bristles. As a result, the 22 hollow nodules whose rims are no longer identifiable are not included in the histogram of rim thickness. The average rim thickness estimated from 491 hollow nodules is 0.25 mm (Table 2), ranging from 0.01 mm to just larger than 1 mm. Rim thickness values also follow a Gaussian distribution between ~0.02 mm and 0.6 mm, with a mode just greater than 0.2 mm (Figure 4e). The distribution as a whole exhibits a slight positive skew due to the presence of several rims thicker than 0.6 mm. A plot of interior hollow diameter versus rim thickness (Figure 5a) shows a linear relationship where increasing interior hollow diameter results in increasing rim thickness with a slope of 0.14. The linear regression model finds this slope to be significant and nonzero despite the large amount of scatter in the data. It was suspected that the two largest interior hollow diameters around 4 mm might be exerting disproportionate influence on the linear fit, but removal of these two points still resulted in a statistically significant, nonzero slope for the linear model suggesting that rim thickness scales with hollow interior diameter (Figure 5b).

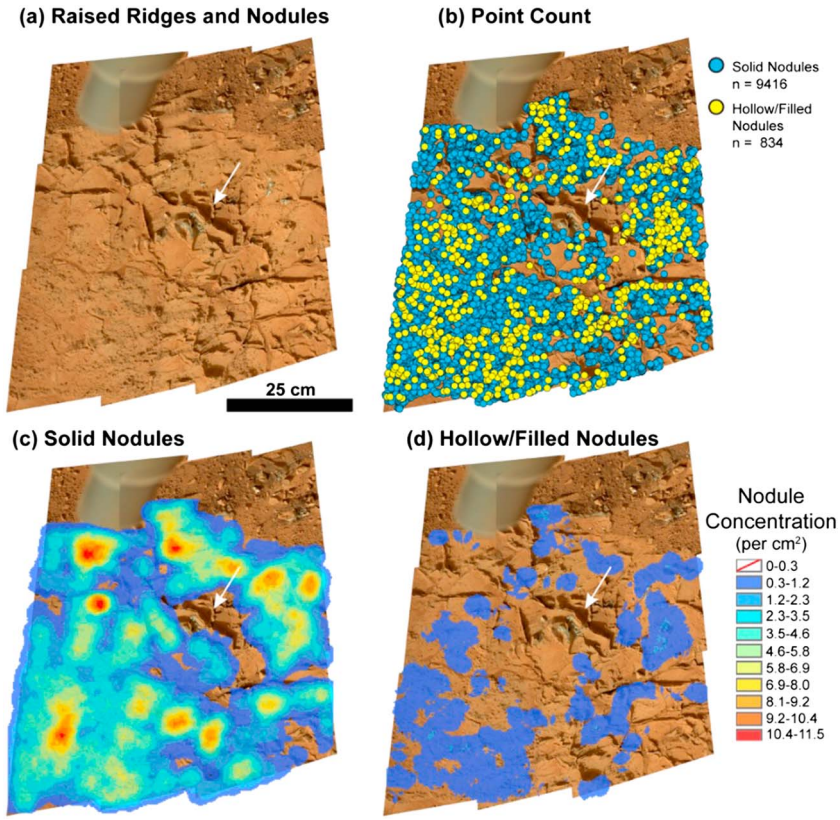

Figure 10. Solid and hollow/filled nodules in the vicinity of a dense network of raised ridges in an M-100 mosaic taken on sol 164. See supporting information for list of image IDs. (a) Raised Ridges and Nodules mosaic. (b) Point count of solid and hollow/filled nodules. (c) Map showing the distribution and concentration of solid nodules. (d) Map showing the distribution and concentration of hollow/filled nodules. White arrows point to an area of the outcrop containing raised ridges but sparse solid and hollow/filled nodules.

3.3. Filled Nodules

Only 30 filled nodules were identified in the 20 MAHLI images listed in Table 1. There are a variety of irregularly shaped white blebs observed in the Sheepbed outcrop, but only those with identifiable raised rims were tabulated as filled nodules. This distinction permits the possibility that secondary porosity could have resulted from fluid migration associated with reprecipitation of calcium sulfate. As noted by *Grotzinger et al.* [2014], filled nodules are usually associated with thin, hairline, mineralized veins that extend radially outward from the raised rim and connect with larger calcium sulfate filled fractures (Figures 2e and 2f). The mean diameter of filled nodules is 2.75 mm, ranging from 1.18 mm to up to 5.15 mm. The small number of filled nodules makes it difficult to interpret size trends, although there appears to be a general decrease in filled nodules with increasing diameter (Figure 4c). The average areal concentration calculated from 11 MAHLI

Table 4. Nearest Neighbor Statistics for Lateral Solid Nodule and Hollow Nodule Distributions

Mosaic	Nodule Type	Observed Mean Distance (mm)	Expected Mean Distance (mm)	Nearest Neighbor Ratio	Pattern
John Klein	solid	2.3	3.2	0.73	Clustered
	hollow/filled	4.9	7.8	0.63	Clustered
Cumberland 1	solid	3.0	3.6	0.82	Clustered
	hollow/filled	4.9	7.0	0.70	Clustered
Cumberland 2	solid	4.3	5.0	0.86	Clustered
	hollow/filled	8.1	10.7	0.75	Clustered
Raised Ridges and Nodules	solid	2.5	3.3	0.76	Clustered
	hollow/filled	7.2	10.8	0.67	Clustered

Table 5. ChemCam Comparison of the Chemistry (wt %) Between the Nodule-Rich Area and Overall Sheepbed Composition

	SiO_2	TiO_2	Al_2O_3	FeO	MgO	CaO	Na_2O	K_2O
Sheepbed (354 points)	46.6	1.1	8.1	16.9	6.3	6.2	2.4	0.6
Nodule-rich area (128 points)	45.7	1	8.2	16.6	5.6	6.5	2.4	0.6

[a]See N. Mangold (Chemical variations of Yellowknife Bay Formation sediments analyzed by the Curiosity Rover on Mars, submitted to *Journal of Geophysical Research*, 2014) for a discussion of the error analysis associated with these values.

images containing filled nodules is 0.7%, although minimum concentration is as low as 0.1% for Brock_Inlier, Autridge, and Cumberland_DRT and as high as 2.2% for Persillon and Drill_RP (Table 1). The average aspect ratio measured for hollow nodule interiors is 1.16, suggesting that these features are generally circular in cross section. Of the 30 hollow nodule interiors measured, 29 (97%) are circular ($AR < 1.5{:}1$), and only 1 (3%) is subcircular ($1.5{:}1 < AR > 2.5{:}1$).

3.4. Statistical Testing

The results of Wilcoxon rank sum testing are presented in Table 3. The null hypothesis that two data sets represent samples from a continuous distribution with equal medians is rejected at a 5% significance level or smaller for all permutations of diameter and aspect ratio comparisons except for one, which compares hollow nodule versus filled nodule aspect ratios. These results suggest that solid nodules and hollow nodules are distinct from each other in size and shape but that hollow nodules and filled nodules likely originate from distributions with equal aspect ratio medians.

3.5. Summary

Three types of nodules are present in the Sheepbed member in order of decreasing abundance: solid nodules, hollow nodules, and filled nodules. Solid nodules outnumber hollow nodules in the MAHLI image set by a factor of 3, and only 30 filled nodules were observed. Although all nodule types are generally circular in cross section and millimeter scale, statistical testing of solid nodule and hollow nodule diameter and aspect ratio confirm that these two nodule types are statistically different in size and shape. Mean hollow nodule diameter is larger than mean solid nodule diameter and the diameter histograms of these two features are distinct; solid nodule diameters follow a lognormal distribution, while the hollow nodule diameters are normally distributed. Hollow and filled nodules show statistically significant differences in size, but the shape of these two nodule types are statistically indistinguishable. Lastly, there is a statistically significant relationship, despite a large amount of scatter, between hollow nodule rim thickness and the diameter of hollow nodule interior voids.

4. Spatial Distribution

4.1. Lateral Distribution

Solid, hollow, and filled nodules are well exposed on relatively flat, bedding plain surfaces of the upper Sheepbed member in the vicinity of the John_Klein and Cumberland drill sites (Figure 3b). Four Mastcam mosaics of these surfaces illustrate the lateral distribution of solid nodules and hollow/filled nodules in the Sheepbed member (Figure 6).

4.1.1. John Klein Drill Site

The John Klein drill site was imaged by the M-100 camera on sol 166 (Figure 7). Solid nodule and hollow/filled nodule point counts of this mosaic reveal that solid nodules and hollow/filled nodules occur across the image scene, albeit in variable concentrations, except in the immediate vicinity of a small network of raised ridges, 5–10 cm long mineralized and spindle-ended fractures, in the top part of the mosaic (Figure 7a). The solid nodule concentration map (Figure 7c) shows several areas of very high concentration in the right part of the mosaic (>12 nodules/cm^2), while the majority of the image scene exhibits relatively medium to low concentrations (<7 nodules/cm^2). The highest concentration of solid nodules, the two red zones in the upper right corner of the image where concentrations are between 15 and 19 solid nodules/cm^2, occurs along an elongate, sublinear raised feature ~30 cm in length that trends from the upper right to lower left. Solid nodules in this area are generally smaller (<1 mm in diameter) than those present in regions of lower concentration. Similarly, the highest concentration of hollow/filled nodules (1.7–2.7 nodules/cm^2) occurs in a small patch located in the lower left corner of the image (Figure 7d). Hollow/filled nodule densities

acrossthe scene range between 0.3 and 1.7 nodules/cm^2. Hollow and filled nodules are conspicuously absent from regions containing raised ridges (Figure 7d). An intermediate concentration of hollow/filled nodules (0.6–1.7 nodules/cm^2) occurs on the right side of the mosaic, coincident with the highest concentration of solid nodules. In the vicinity of the actual John_Klein drill hole, solid nodule concentration is 3.8–5.3 nodules/cm^2 and hollow/filled nodule concentration is 0.6–1.7 nodules/cm^2.

Average nearest neighbor statistics (Table 4) reveal that both nodules and hollow/filled nodules are clustered in the outcrop surface, rather than occurring in a random or dispersed pattern. This means that the ratio of measured distance between nodules to expected distance for nodules that are randomly distributed is less than one. The observed mean distance between solid nodules is 2.3 mm, smaller than the expected mean distance of 3.2 mm for a hypothetical random distribution, and the observed mean distance between hollow/filled nodules is 4.9 mm, smaller than the expected distance of 7.8 mm for a random distribution.

4.1.2. Cumberland Drill Site

Mastcam mosaics taken by the M-100 camera on sols 185 (Cumberland 1) and 275 (Cumberland 2) (Figures 8 and 9) cover the Cumberland drill location and surrounding region. The concentration map of the Cumberland 1 mosaic reveals an area of particularly high solid nodule (10–12 nodules/cm^2) and hollow/filled nodule (2–3 nodules/cm^2) concentration in the lower left corner of the mosaic (Figure 8c). This region corresponds with an area that appears slightly raised compared to the broader surface and may represent a region of enhanced resistance from erosion resulting from the high concentration of nodules. The area just below and to the right of this high concentration area contains few nodules (Figures 8c and 8d). Solid nodules do not occur in concentrations higher than 5–6 nodules/cm^2 across the rest of the image, but there are several areas of relatively high hollow/filled nodule concentration (1–2 nodules/cm^2) along the flagstone edge on the right side of the mosaic (Figure 8d).

The Cumberland 2 mosaic (Figure 9) includes the Cumberland drill site, chosen for its apparent high concentration of hollow nodules. However, the hollow/filled nodule concentration in the vicinity of the actual drill hole is 0.3–0.7 nodules/cm^2 (Figure 9d), an intermediate to low concentration according to the concentration map; the highest concentration of hollow/filled nodules occurs in the upper left portion of the mosaic (0.7–1.4 nodules/cm^2). The rest of the mosaic contains a fairly low concentration of hollow/filled nodules (0–0.7 nodules/cm^2), especially in the area just below the Cumberland drill area on the Mastcam image. The solid nodule point count (Figure 9c) shows the highest concentration (4–7 nodules/cm^2) in a linear pattern trending from the upper left to the lower right in the upper right portion of the mosaic. Besides this area of relatively high solid nodule concentration, most of the mosaic contains a low concentration of solid nodules ($<$2 nodules/cm^2).

Average nearest neighbor statistics reveal that the distribution of solid nodules and hollow/filled nodules in the Cumberland mosaics, as with the John Klein site, is clustered (Table 4). For both Cumberland mosaics, the observed mean distance between solid nodules and hollow/filled nodules, respectively, is smaller than the expected mean distance for a hypothetical random distribution.

4.1.3. Raised Ridges and Nodules

The Raised Ridges and Nodules mosaic taken by the M-100 camera on sol 164 (Figure 6) was chosen to explore the spatial distribution of nodules with respect to a network of raised ridges. Point counting reveals that solid nodules and hollow/filled nodules are present around and between some of more sparsely distributed raised ridges, but there are few, if any nodules where the network of raised ridges is relatively dense (Figures 6c and 6d). Hollow/filled nodules are particularly sparse in these regions (Figure 6d). As with several of the mosaics, the areas of highest solid nodule concentration (containing between 10 and 12 nodules/cm^2) generally contain smaller nodules ($<$1 mm) than those areas with lower concentrations.

Average nearest neighbor statistics reveal that the distributions of solid nodules and hollow/filled nodules in this mosaic are clustered, as opposed to random or dispersed (Table 4). The observed mean distance between solid nodules is 2.5 mm, smaller than the expected mean distance of 3.3 mm. The observed mean distance between hollow/filled nodules is 7.2 mm, smaller than the expected distance of 1.1 cm.

4.2. Vertical Distribution

The vertical distribution of nodules is best observed at a 0.5 m thick exposure of the Sheepbed member, informally named the Selwyn section, located ~5 m southwest of the John_Klein drill site (Figures 1 and 6).

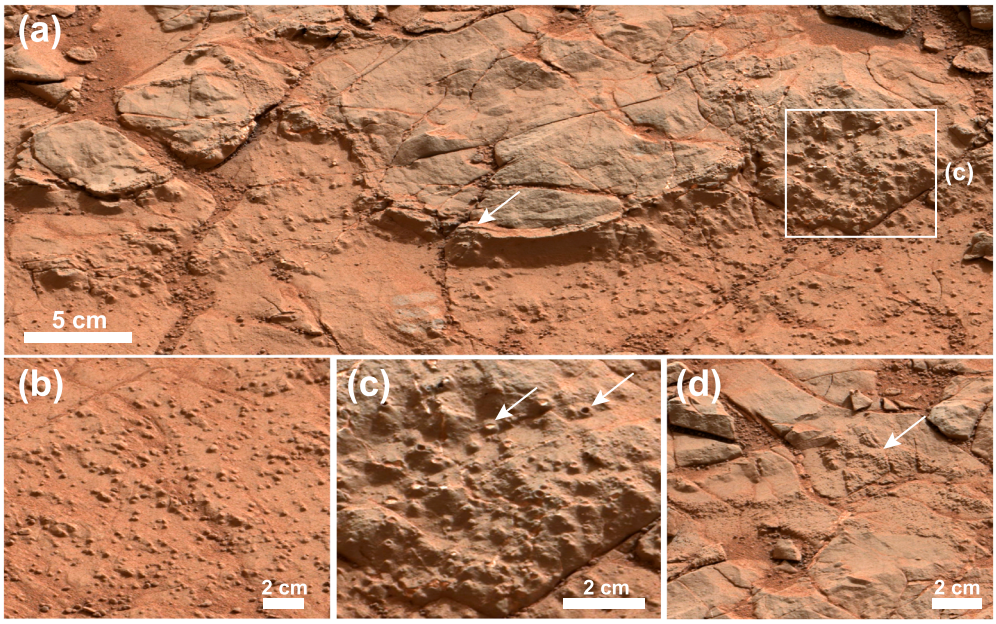

Figure 11. Selwyn M-100 mosaic taken on sol 159. See supporting information for list of image IDs. (a) The irregular boundary between the upper and lower Sheepbed member. Arrow points to the poorly developed raised ridge that defines this boundary. (b) Large (>1 mm) solid nodules and hollow nodules characteristic of the lower Sheepbed member. (c) Large (>1 mm) filled and hollow nodules at the boundary between the upper and lower Sheepbed. Left and right arrows point to a filled and hollow nodule, respectively. (d) High-concentration area of very small solid nodules (<1 mm) indicated by the white arrow that is characteristic of the upper Sheepbed.

Here the rover traversed the most vertically complete section of the Sheepbed mudstone from sols 150 to 167 and again on sols 296–300 during the exit from Yellowknife Bay.

4.2.1. Selwyn

The Selwyn mosaic, obtained by the M-100 camera on sol 159, shows a ~15 cm thick interval of the 50 cm thick Selwyn section (Figures 11 and 12). This mosaic captures an irregular boundary defined, in part, by a poorly developed raised ridge and a high concentration of large hollow nodules and filled nodules (Figure 11a). *McLennan et al.* [2014] also identified this boundary as a compositional distinction between the "lower" and "upper" parts of the Sheepbed member. Stratigraphically lower strata exhibit lower and more variable TiO_2/Al_2O_3 and less Ni than the stratigraphically higher interval, suggested to represent a subtle change in provenance [*McLennan et al.*, 2014]. Below this boundary, the Sheepbed member is distinctly red in color (although this likely results from the distribution of windblown dust) and contains abundant large nodules greater than 1 mm in diameter (Figure 11b). The upper Sheepbed appears gray in color and contains nodules generally less than 1 mm in diameter (Figure 11d versus Figure 11b). Although the nodules in the stratigraphically lower part are larger and more conspicuous, the highest concentration of nodules actually occurs in the upper Sheepbed, where several irregular patches of very small (<1 mm) solid nodules and hollow/filled nodules occur (Figure 12c). Hollow/filled nodules are concentrated at the boundary between the upper and lower Sheepbed and in a patch of large, dense nodules on the left side of the mosaic (Figures 11c and 12d). This mosaic also contains a large number of loose pebbles accumulated in cracks and on the outcrop surface. Upon close inspection, many, but not all, pebbles contain small dimples or depressions, suggesting they are eroded remnants of hollow nodules.

4.2.2. Yellowknife Bay Egress

An M-100 mosaic obtained on sol 298 shows the Sheepbed-Gillespie Lake contact as imaged during Curiosity's egress from Yellowknife Bay (Figure 13). This section occurs approximately 2 m to the southwest of the Selwyn section and mcam00864 (Figures 6 and 13). The mosaic covers a 35 cm thick interval of the Sheepbed member, although the lower portion of the outcrop is discontinuous and the blocks near the bottom of the image may be out of place. Solid nodules are present throughout the section, but hollow/filled nodules are sparse in this part of the Sheepbed member. Solid nodules are largest (~1 mm) and most clearly

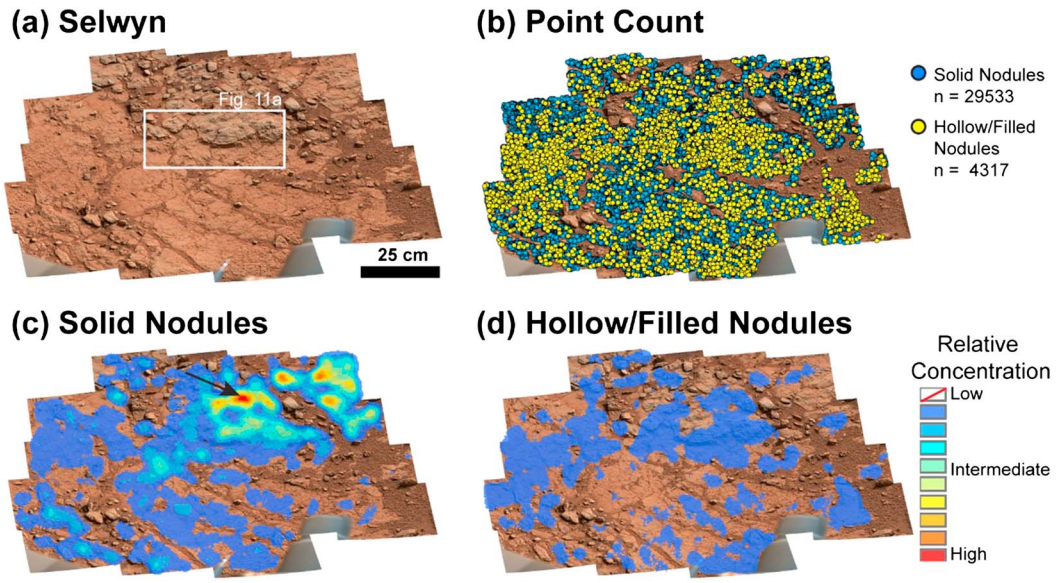

Figure 12. Solid nodules and hollow/filled nodules distributed vertically through the Selwyn section in the vicinity of the lower to upper Sheepbed transition in an M-100 mosaic taken on sol 159. See supporting information for list of image IDs. (a) Selwyn mosaic. (b) Point count of solid and hollow/filled nodules. (c) Map showing the distribution and concentration of solid nodules across the lower to upper Sheepbed boundary. Black arrow points to an area of high solid nodule concentration in the upper Sheepbed. (d) Map showing the distribution and concentration of hollow/filled nodules through the Sheepbed.

observed in a ~10 cm thick interval near the center of the mosaic that is pervasively cut by mineralized white veins. However, the highest concentration of solid nodules occurs in two small, irregularly shaped patches just below the Sheepbed-Gillespie boundary. Solid nodules in these patches are smaller ($<$1 mm) than solid nodules present elsewhere in the mosaic.

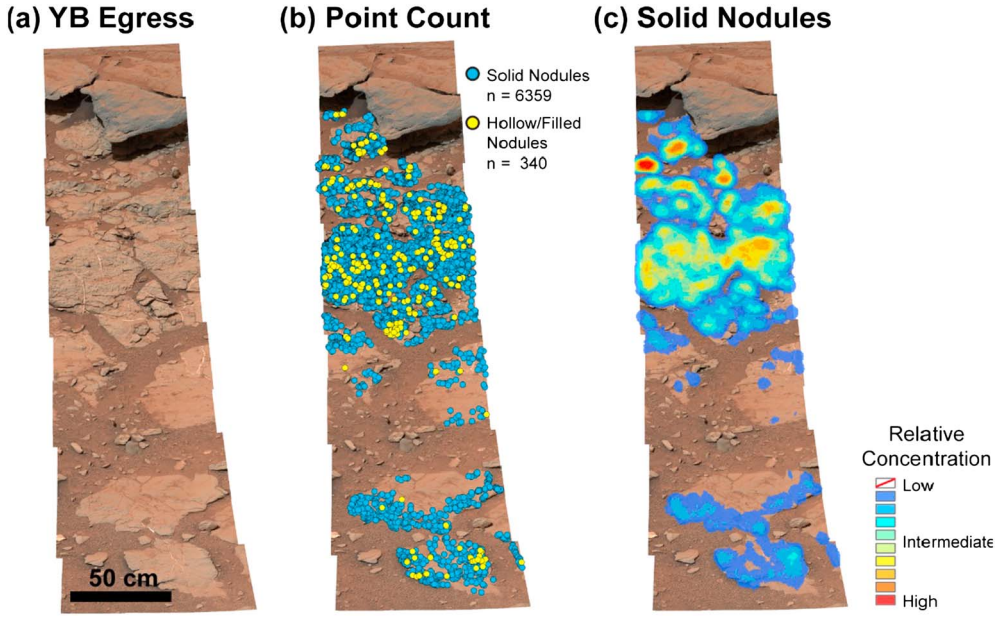

Figure 13. Solid and hollow/filled nodules distributed vertically through the Sheepbed in the Yellowknife Bay (YB) Egress mosaic taken with the M-100 camera on sol 298. See supporting information for list of image IDs. (a) Yellowknife Bay Egress mosaic. Overhanging blocks at the top of the image mark the Sheepbed-Gillespie contact. (b) Point count of solid and hollow/filled nodules. (c) Map showing the distribution and concentration of solid nodules through the Sheepbed. Due to the low concentration of hollow/filled nodules in the scene, a map was not created for the hollow/filled nodules.

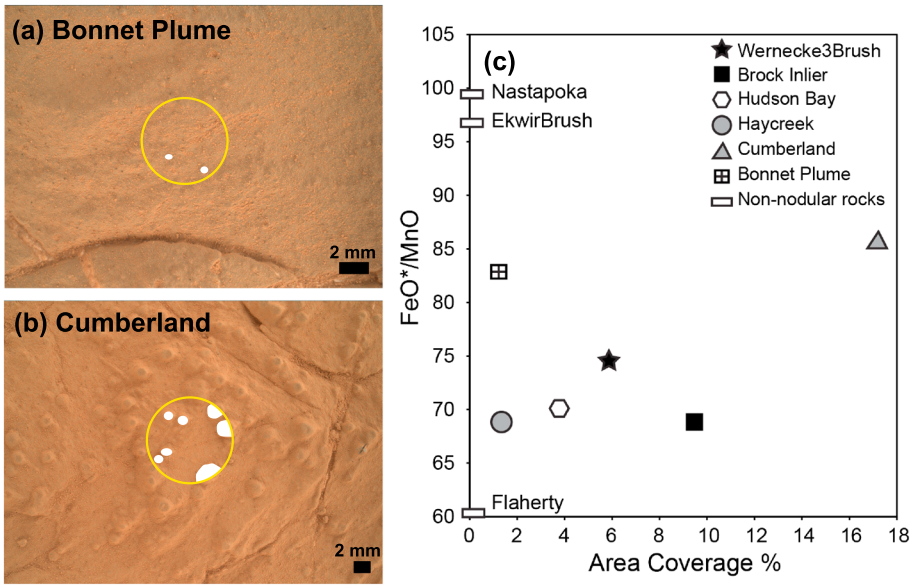

Figure 14. (a) MAHLI focus merge product (0161MH0001920000101910R00) showing target Bonnet Plume. Yellow circle shows the area analyzed by APXS. White shapes represent nodules (both solid and hollow/filled nodules). (b) MAHLI focus merge product 0276MH0002650000103019R00 showing the Cumberland drill site before it was drilled. Yellow circle shows the area analyzed by APXS. (c) Plot of nodule areal coverage in the APXS field of view vs. FeO*/MnO as determined by APXS.

4.3. Summary

The six Mastcam maps presented here show that solid and hollow/filled nodule distributions are patchy and statistically clustered both laterally and vertically throughout the examined portions of the Sheepbed member. Solid nodules outnumber filled/hollow nodules by factors of 4 to 20 in the Mastcam mosaics examined in this study, although there is likely some bias toward solid nodule identification resulting from the lower resolution of the Mastcam mosaics (Figures 7–13). Different nodule types coexist throughout these outcrops, but areas of highest solid nodule concentration do not always coincide with areas of highest hollow/filled nodule concentration. Solid nodules and hollow/filled nodules, in particular, are not present in high concentrations in the immediate vicinity of dense raised ridge networks.

5. Chemical Composition of the Sheepbed Nodules

5.1. APXS

Nodules (solid, hollow, and filled tabulated together) account for ~2 to 17% of the area analyzed by APXS within the instrument FOV at the six nodule-bearing targets (Figure 14). There is no apparent correlation between the abundance of nodules and most elemental abundances, such as Si, Al, or S. However, there is an apparent correlation between nodule abundance and FeO* (in which FeO* assumes all Fe is present as FeO.) and MnO concentration in nodule-bearing targets, particularly when these oxides are ratioed (Figure 14c). This correlation suggests that precipitation of Fe-oxide may have been involved in nodule formation. Possible iron-bearing cementing minerals are magnetite (Fe_3O_4), present as 3.8 and 4.4 wt % of the John Klein and Cumberland drill powders, respectively [*Vaniman et al.*, 2014], or akageneite ($Fe^{3+}O(OH,Cl)$), observed at 1.1 and 1.7 wt % in the John Klein and Cumberland drill powders, respectively. However, the APXS data show no obvious correlation between Cl and nodule-bearing areas, as might be expected for akaganeite. Hematite is present in the drill samples at or near the detection limit of the CheMin instrument (0.6 wt % in John Klein, 0.7 wt % in Cumberland), so hematite is not considered to be the likely cementing mineral given the abundance of nodules within the Sheepbed member. An important caveat of the iron enrichment observed in APXS analyses of nodule-bearing targets is the high degree of variability that exists in the FeO*/MnO of nodule-free rock targets, which may be related to stratigraphic variations in rock composition [*McLennan et al.*, 2014], such as from disseminated Fe-oxides within the mudstone matrix. The rock targets Bonnet Plume and nodule-free Nastapoka both have a darker appearance and FeO*/MnO ratios between 80 and 100 (Figure 14) consistent with this interpretation.

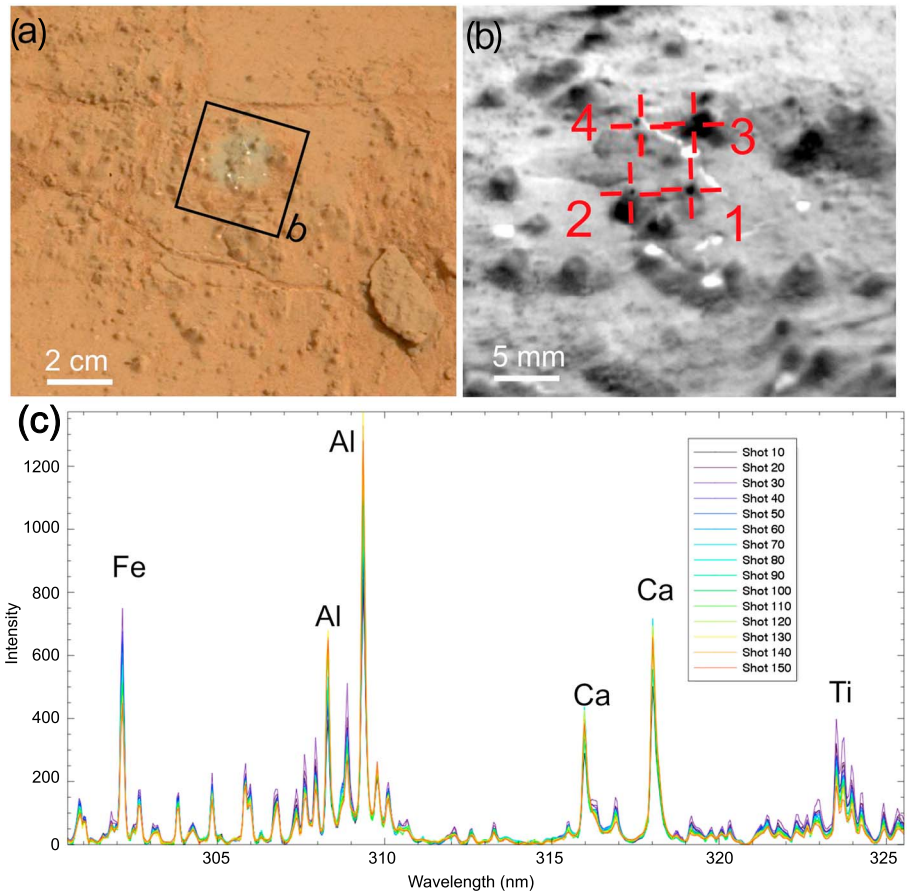

Figure 15. Mastcam image 0166MR0008880120201641E01 in the vicinity of the John Klein drill showing the gray, dust-free area blasted by the ChemCam laser shots. (b) ChemCam/RMI image of target DT-RP5 (CR0_412227292EDR_F0052270CCAM01166M) after the four depth profiles were performed. (c) Portion of the ChemCam spectra on location 2 showing the spectra of every tenth shot. The higher emission lines of Ca and Al for reddish spectra show an enrichment at depth.

5.2. ChemCam

During the ChemCam depth profile experiment at targeted observation DT-RP5, the laser hit filled nodules in the three first locations of the 2×2 depth profile array, although contact was only on the filled nodule edge for points 1 and 3. In contrast, the second location shows a clear ablation hole coincident with a nodule center (Figure 15). ChemCam data on locations 1 and 3 do not show significant compositional variation beyond dust contamination in the first shots. Location 2, however, records distinct variations in Ca and Al (Figure 15c). Over a large number of shots, the plasma becomes progressively confined to the pit it creates, leading to a general decrease of the total emission, and an associated decrease of all element emission lines. This is observed in the case of location 2 for most emission lines (and illustrated for Fe and Ti in Figure 15), and no increase in H is detected that would suggest a specific hydrous phase. By contrast, Ca and Al emission does not drop along with the other elements, suggesting these elements are enriched at depth, perhaps in the interior of the filled nodule. These small changes could be part of the natural variability of the overall rock, and it is a possibility that the ablation cavity was not deep enough to reach the interior of the nodule. Therefore, the depth profile experiment with ChemCam does not uniquely support a contrast between the composition of the mudstone and the composition of the nodules analyzed.

ChemCam data recorded in Table 5, which represents a comparison between nodule-free Sheepbed mudstone and the average of 128 nodule-bearing shot locations, suggest that the composition of the Sheepbed mudstone in nodule-rich areas is not distinct from the overall composition of the Sheepbed mudstone observed over the broader expanse of Yellowknife Bay. For instance, no enrichment in Fe is observed in the nodule-rich areas. Only minor differences exist between data sets, such as a slight depletion

in the nodule-rich areas in Mg, and a slight enrichment in Ca. The latter could result from the presence of filled nodules containing Ca-sulfates [*Grotzinger et al.*, 2014; M. Nachon, Calcium sulfate veins characterized by ChemCam/Curiosity at Gale crater, Mars, in revision *Journal of Geophysical Research*, 2014].

In summary, these observations indicate that the filled nodules are indeed associated with calcium sulfate minerals but do not help to identify a specific composition for the primary nodule-forming cement. ChemCam data show no enrichment in iron that could confirm the presence of magnetite, akaganeite, or other distinct Fe minerals.

5.3. Summary of Geochemical Results

APXS analyses presented here show that nodule-rich areas correlate with FeO* concentration, particularly when FeO* is ratioed with MnO. This correlation suggests that solid, hollow, and filled nodules may contain a higher concentration of an iron-bearing mineral than the host mudstone. These APXS results are consistent with the CheMin detection of the Fe-oxide minerals magnetite and akaganeite at the John_Klein and Cumberland drill sites [*Vaniman et al.*, 2014], although APXS cannot conclusively identify the specific iron-bearing mineral due to the potential contribution of dust to the analysis.

Unlike APXS, ChemCam does not detect any correlation between Fe and nodule abundance (Table 5), although this disparity is not unexpected given the difference in analytical capabilities of the two instruments. The typical 30 shots that comprise a ChemCam analysis may not provide enough penetration ($<$100 μm) into the nodules to observe a conclusive elemental enrichment. In addition, the ChemCam depth profiles (150 shots, or $>$100 μm penetration) have only locally penetrated the interiors of filled nodules whose compositions may not be representative of solid or hollow nodules. Although ChemCam data do not show an Fe-enrichment of the nodules indicated by both APXS and CheMin, they do suggest that compositional difference between the host mudstone and the nodules is quite subtle.

6. Discussion

6.1. Petrogenesis of Sheepbed Nodules

Several processes could result in millimeter scale, spherical textural elements in Martian sedimentary rocks. Potential explanations for the Sheepbed nodules include accretionary sedimentary grains, impact or volcanic accretionary lapilli, impact or volcanic glass spherules, or diagenetic concretions [*Grotzinger et al.*, 2014]. Sheepbed nodules distinctly lack internal concentric growth bands, which eliminates an accretionary sedimentary origin as ooids or pisoids. Lack of concentric growth bands also suggests that an origin as volcanic or impact accretionary lapilli is unlikely. *Fralick et al.* [2012] distinguish impact accretionary lapilli deposits by the presence of ubiquitously associated breccias deposited during ground movement and entrainment of debris in the leading edge of impact-induced base surges. No such deposits have been identified in the Sheepbed mudstone or any other member of the Yellowknife Bay formation. Furthermore, accretionary grains deposited in fluvial-lacustrine settings inferred for the Sheepbed member and overlying Gillespie Lake member would be expected to exhibit hydraulic sorting or segregation of spherules by size; Sheepbed nodules and hollow nodules are neither graded nor concentrated.

An origin for the Sheepbed nodules as volcanic melt spherules is also unlikely. Volcanic melt spherules on Earth generally occur with other nonspheroidal particles [*Simonson*, 2003; *Simonson and Glass*, 2004], which is not supported by the strongly spherical aspect ratios of nodules in the Sheepbed member. An origin as impact spherules, spheroidal molten particles that form from the melting and vaporization of material during an impact [*Simonson and Glass*, 2004] may be more consistent with the characteristics of Sheepbed nodules. The Sheepbed nodules, like impact melt spherules, are dominantly spheroidal, less than 5 mm in diameter, and smaller nodules (1–2 mm) tend to be more spherical [*Simonson and Glass*, 2004].The subtle chemical signature of the nodules makes it impossible to eliminate an impact spherule origin based solely on composition, as *McLennan et al.* [2005] did for the Meridiani hematite spherules. Furthermore, a generally diverse suite of internal structures commonly used to distinguish impact melt spherules cannot be used to evaluate the origin of Sheepbed nodules. However, it is unlikely that glassy spherules—of either volcanic or impact origin—would be preserved in outcrop given that aqueous conditions during or soon after Sheepbed deposition resulted in the near complete alteration of olivine to smectite clay minerals [*Vaniman et al.*, 2014].

Additionally, possible impact spherules have been identified in the modern Rocknest eolian sediments of Gale crater [*Minitti et al.*, 2013], and these spherules differ from nodules within the Sheepbed member in several important ways. Impact spherules documented within the Rocknest deposit are typically substantially smaller (ranging from 100 to 800 μm in diameter) than the nodules described here and are distinctly spherical (with aspect ratios indistinguishable from 1.0). Additionally, observed spherules preserve a glassy luster, which results in a uniform distribution of light reflection off of the grain surface. This is very different from the grainy texture of nodules within the Sheepbed mudstone. Finally, the impact spherules observed in Gale occur dominantly within unlithified surficial sediment [*Minitti et al.*, 2013], although there are several potential examples within coarser, well-lithified sandstone units (Newsom et al., in revision). Regardless, observed impact spherules appear sparsely distributed within Gale crater materials. In terrestrial examples, spherules commonly occur as discrete event beds that are laterally extensive and can remain undiluted by other detrital grains for hundreds to thousands of kilometers [*Simonson*, 2003; *Fralick et al.*, 2012]. This would be true especially for depositional facies originating from settling of grains from suspension, as inferred for the Sheepbed mudstone. Nodules in the Sheepbed member do not occur in distinct beds and are patchily distributed both vertically and horizontally throughout the outcrop, inconsistent with the characteristics of an impact spherule layer. Finally, impact spherules deposited in a potentially lacustrine environment should also show normal grading and uniform thickness [*Fralick et al.,* 2012]. The Sheepbed nodules and hollow nodules are neither graded nor present in beds of uniform thickness, so an origin as impact melt spherules is unlikely.

Precipitation of authigenic minerals from diagenetic pore fluids to form concretions is the most parsimonious interpretation for the origin of Sheepbed nodules. Their size, shape, distribution, and depositional setting are all consistent with concretion formation in fluid-saturated, fine-grained sediments [e.g., *Chan et al.*, 2004; *McLennan et al.*, 2005; *Calvin et al.*, 2008]. Also, the nearly ubiquitous coexistence of solid, hollow, and filled nodules throughout the Sheepbed member suggests that these nodules share a common concretionary origin. Mechanisms of concretionary growth that can account for the full range of observed nodule morphology are explored further below.

6.2. Controls on Nodule Shape and Size

Solid, hollow, and filled nodules in the Sheepbed member reveal near-circular geometries in geometrically diverse outcrop exposure, indicating that all nodule types are predominantly spherical in three dimensions. Concretionary bodies generally form spherical shapes when cementing ions are supplied by diffusion to single-point nucleation sites [*Bjørkum and Walderhaug*, 1990; *McBride et al.*, 1994, 1999; *Chan et al.,* 2004], as opposed to either diffusion to nonpoint nucleations or ion supply by advection, both of which tend to form elongate concretions. In the case of advection, elongate concretions provide a measure of the direction of fluid flow [*Schultz*, 1941; *McBride et al.*, 1994; *Chan et al.*, 2012]. Alternatively, spherical concretion growth has also been interpreted to result primarily from surface reactions, in which each unit surface area has the same growth rate during surface reaction-controlled growth [*Bjørkum and Walderhaug*, 1990; *Raiswell*, 1988]. Accordingly, the spherical shape of the Sheepbed nodules suggests that a combination of diffusion and/or mineral surface reactions influenced nodule cementation but in the absence of either strongly oriented nucleation surfaces or groundwater flow.

The shape of concretions on Earth has also been linked to sediment permeability and variations in the local availability of cementing agents. Anisotropic permeability is thought to result in elongate and preferentially oriented concretions [*Sorby*, 1908; *Deegan*, 1971; *Gluyas*, 1984; *Dix and Mullins*, 1987; *Hudson and Andrews*, 1987; *Seilacher*, 2001; *Chan et al.*, 2012]. Oriented concretions can also form due to differential concentrations of cementing agents in the vertical or horizontal directions [*Bjørkum and Walderhaug,* 1990]. Since Sheepbed nodules are generally spherical and do not appear to be preferentially oriented, the Sheepbed sediments were likely homogeneous at the scale of individual nodule sites, exhibiting local isotropic permeability and a uniform distribution of cementing ions.

Sediment and fluid properties can also influence concretion size [*Chan et al.*, 2004]. The abundance of nodules in the Sheepbed member indicates a scenario in which a high density of nucleation sites formed within the sediments. However, the small mm-scale size of the nodules suggests that transport of fluids and/or diffusion of cementing ions to these nucleation sites may have been limited, perhaps by the low permeability of clay-rich Sheepbed sediments. Slight variations in the porosity and permeability of the upper and lower Sheepbed may explain the abundant growth of numerous small nodules (<1 mm) in the upper Sheepbed versus fewer but larger nodules (>1 mm) in the lower Sheepbed (Figures 11b, 11c, and 11d).

Measurements of solid and hollow nodule diameter and aspect ratio indicate that models for nodule growth should take into account size and shape statistics as well as morphological characteristics. Hollow nodule growth mechanisms should be consistent with the uniform size and shape distributions of both whole hollow nodules and hollow nodule void interiors (Figure 4), as well as the subtle relationship between interior void diameter and hollow nodule rim thickness (Figure 5) which suggests that interior void generation is linked to the growth of hollow nodule rims.

Comparison between hollow and filled nodule size statistics is hindered by the small sample size of filled nodules, but Wilcoxon rank sum testing and the morphological similarities between hollow and filled nodules are consistent with *Grotzinger et al.*'s [2014] interpretation of filled nodules as hollow nodules that have been filled during later diagenesis. The size difference between hollow nodules and filled nodules suggests that larger hollow nodules may have been more susceptible to later diagenetic fracturing and fluid flow that led to the precipitation of sulfate minerals within hollow nodule interiors.

6.3. Controls on Nodule Spacing

Nearest neighbor statistics show that solid nodules and hollow/filled nodules are nonuniformly and nonrandomly clustered both laterally and vertically throughout the Sheepbed member. The occurrence of nodules in irregular patches rather than beds is one of the strongest lines of evidence supporting a diagenetic concretionary origin for the nodules. Clustered distributions of concretions are thought to be the result of several factors, including the presence of favorable nucleation sites controlled by heterogeneities in sediment permeability or chemical composition, or the influence of concretions on each other [*Raiswell and White,* 1978]. Examples of such heterogeneities at the cm-scale can be observed at the Selwyn section. The presence of a raised ridge and a high concentration of nodules (Figure 11) coincides with a compositional transition between the upper and lower Sheepbed. APXS analyses from the lower Sheepbed at the Selwyn section show that this interval exhibits lower Al_2O_3/TiO_2 and lower Ni than the upper Sheepbed at Selwyn [*McLennan et al.*, 2014]. These geochemical differences, which *McLennan et al.* [2014] attribute to subtle changes in sediment provenance, coupled with permeability variations discussed in the previous section could have influenced the development of a diagenetic front at the upper-lower Sheepbed boundary.

Sedimentary structures including bedding or bedforms can also influence the development of concretions, although the generally uniform and massive nature of the Sheepbed member makes such control on the distribution of nodules and hollow/filled nodules unlikely. In the few locations where thin intercalated beds are present [*Grotzinger et al.*, 2014], bedding does not appear to influence the size, shape, or distribution of nodules. However, raised ridges appear to have an antithetical relationship with nodules. This is mostly clearly evident in the point counts and concentration maps of the John Klein and the Raised Ridges and Nodules mosaics (Figures 7 and 10) where solid nodules and particularly hollow/filled nodules are absent where dense networks of raised ridges occur. Two possible scenarios can explain this relationship: (1) nodules and raised ridges formed contemporaneously, but their respective distributions were controlled by rheological or compositional variations within the Sheepbed sediments, or (2) nodules and raised ridges formed at different times, but the prior existence of one type of feature prevented the uniform distribution of the other type of feature, perhaps through the restriction or concentration of diagenetic fluids nonuniformly throughout the outcrop. Distinguishing between these scenarios requires an evaluation of potential growth mechanisms for solid and hollow/filled nodules, which is discussed in detail below.

6.4. Growth of Solid Nodules

The conventional model for concretionary growth involves the passive precipitation of a cementing phase in sediment pore spaces in a concentric, accretionary pattern that radiates outward from a central nucleation point [*Dana*, 1863; *Newberry*, 1873; *Tomkieff,* 1927; *Galimov and Girin*, 1968; *Knoke,* 1966; *Raiswell*, 1971; *Criss et al.*, 1988]. However, the recognition of replacive, displacive, and incomplete cementation textures in concretions indicates that passive precipitation within pore space alone is likely an oversimplification [*Raiswell and Fisher*, 2000]. An alternative model for concretionary growth in mudrocks involves pervasive, rather than concentric growth [*Mozley*, 1996; *Raiswell and Fisher*, 2000]. In this model, individual nuclei—that will eventually form a single concretion—grow concentrically so that a cluster of crystals forms a solid, framework over time [*Raiswell and Fisher*, 2000]. Pervasive growth is capable of leaving significant porosity throughout the volume of the concretion that could be filled with later cements.

The Sheepbed solid nodules show no evidence for internal concentric layering, the most diagnostic evidence for the conventional concentric growth model. However, conclusively distinguishing between the concentric versus pervasive modes of growth–particularly in the absence of of clear concentric zonation-requires microscale textural evidence not attainable with the payload of the Curiosity rover. With this caveat considered, the pervasive growth model may be most consistent with the subtle compositional difference observed in APXS and ChemCam data between the solid nodules and host Sheepbed mudstone. *Raiswell and Fisher* [2000] suggest that concretions forming by pervasive growth contain relatively small amounts of cement in the early stages of growth and thus often retain physical and compositional properties very similar to the host sediment.

6.5. Growth of Hollow Nodules

The patchy distribution of hollow nodules within the Sheepbed member, the variable rim and void morphologies, occurrence of conjoined forms, and co-occurrence of solid nodules and hollow nodules is consistent with a diagenetic concretionary origin for the hollow nodules. However, no straightforward analog for concretion formation on Earth explains the presence of the central void that characterizes Sheepbed hollow nodules. Therefore, three competing hypotheses for the origin of hollow nodule interior voids are considered: (1) hollow nodule voids represent scour pits resulting from preferential erosion at the outcrop surface of a less well-cemented concretion interior, (2) hollow nodule voids represent secondary porosity caused by the dissolution and selective leaching of a more soluble mineral phase that once existed in the center of the nodule, or (3) voids within the hollow nodules represent primary porosity created by the exsolution of gas bubbles from saturated pore fluids in unlithified Sheepbed sediments. Exsolved gas bubbles would then have served as nucleation sites for the precipitation of concretionary rims. The latter two hypotheses were originally proposed by *Grotzinger et al.* [2014] but are evaluated in further detail here using the data presented in this study.

There is no geochemical or visual evidence that a precursor mineral phase once occupied the hollow nodule voids, but the absence of a present-day interior phase does not preclude the possibility that one may have existed. Therefore, the first two models evaluated here consider the possibility that material, whether similar to the host sediment or a distinct mineral phase, once existed within the hollow nodule voids but was later removed at the surface by erosion (hypothesis 1), or at depth by dissolution (hypothesis 2). According to the first hypothesis, Sheepbed hollow nodules would have formed originally as differentially cemented concretions whose less well-cemented interiors eroded at the present-day outcrop surface to form the interior voids. Differentially cemented concretions have been documented on Earth, and *Mozley and Davis* [2005], for example, described "composite concretions" from the Sante Fe Group, New Mexico. At this locality, some concretions are completely cemented, while others contain uncemented sand in their interiors. Differentially cemented composite concretions are thought to form by pervasive growth wherein a reaction front forms at the margins of a zone of pore-water whose chemistry is favorable for cement precipitation [*Mozley and Davis*, 2005]. If this reaction front remains stationary for an extended period of time, a strongly cemented rim could form around a weakly cemented interior. Differentially cemented "rind concretions" are also observed in the Jurassic Navajo Sandstone of the southern Utah and northern Arizona [*Potter et al.*, 2011; *Chan et al.*, 2012]. Rind concretions exhibit a well-cemented zone containing hydrous ferric oxides surrounding a cement-poor interior and are variably interpreted to have formed by pervasive, but incomplete, growth in zones of diffusive mass transfer [*Potter et al.*, 2011].

If the Sheepbed hollow nodules were once differentially cemented concretions, it is possible that exposure at the present-day surface could result in the preferential erosion of less well-cemented interiors. However, the presence of filled nodules in the Sheepbed member, interpreted here and in *Grotzinger et al.* [2014] as hollow nodules filled during later diagenesis, suggests that the hollow nodule voids existed prior to their exposure at the present-day outcrop surface. The sulfate-filled fractures observed leading into and out from the filled nodules are consistent with an origin as hydraulic fractures formed in the burial regime under high hydrostatic pressures [*Grotzinger et al.,* 2014]. In this case, extraction of hollow nodule core material would be required to have occurred in the subsurface, before later fracturing and infilling with sulfate minerals, making it unlikely that hollow nodule voids were formed by the preferential weathering of differentially cemented concretions at the present-day outcrop surface.

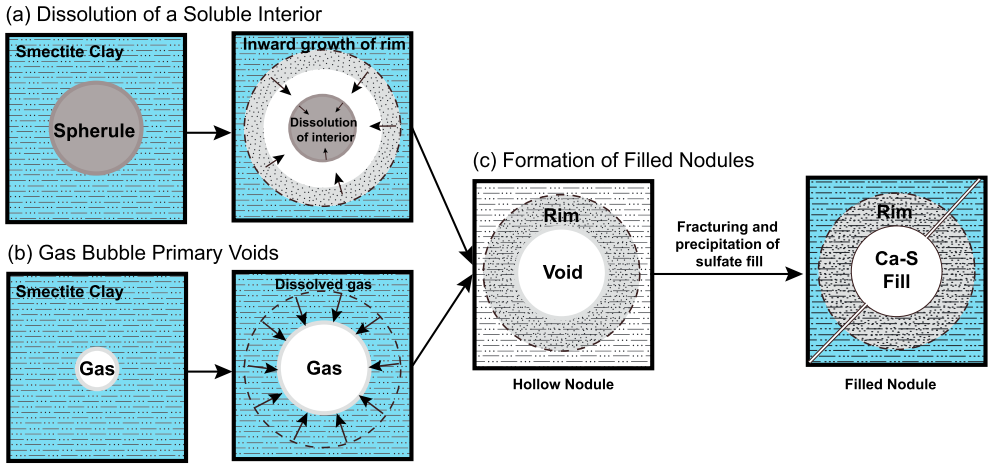

Figure 16. Two models for hollow nodule and filled nodule formation. (a) Model in which hollow nodule voids are produced by the dissolution of a soluble interior during changing redox conditions. In this model, spherules form during early diagenesis of the Sheepbed mudstone. Changing redox conditions result in the dissolution of the spherule at the expense of an inwardly growing rim. (b) Gas bubble model for hollow nodule interior void formation. Dissolved gases exsolve from saturated pore fluids to form bubbles in the Sheepbed mudstone. As bubbles grow by diffusion and incorporation of exsolved gas, the pore fluid chemistry changes in an area immediately surrounding the growing gas bubble. These pore fluid changes create a zone around the bubble favorable for precipitation of an early diagenetic cement, likely an Fe-bearing mineral. Preferential cementation around the bubble creates a resistant rim, which preserves and protects the interior void space from subsequent compaction. (c) Filled nodules form when some hollow nodules experience a later stage of fracturing and interaction with calcium and sulfate-bearing diagenetic fluids that results in the precipitation of calcium sulfate fills in the interior void of some hollow nodules.

The second possibility is that hollow nodule voids represent secondary porosity caused by the dissolution or selective leaching of a more soluble mineral phase that once existed in the cores of the hollow nodules (Figure 16a). Iron oxide-cemented rinds in concretions of the Cretaceous Dakota Formation [*Loope et al.*, 2012], the Navajo sandstone [*Kettler et al.*, 2011; *Loope et al.*, 2012], and Quaternary sediments in the Netherlands [*Van der Burg*, 1969, 1970] are interpreted as forming during the dissolution of early diagenetic siderite spherules caused by changing redox conditions [*Loope et al.*, 2012]. In cohesive muddy sediments, siderite nodules grow displacively, and subsequent oxidation of these nodules during diagenesis leaves behind an iron oxide rind surrounding a central cavity [*Loope et al.*, 2012]. In theory, dissolution-precipitation reactions like that involving siderite during changing redox conditions could produce morphologies similar to those observed in the Sheepbed hollow nodules. In such a scenario, spherules precipitated during early diagenesis of the Sheepbed mudstone would have been dissolved by a later phase of aqueous alteration involving oxidizing pore fluids, thereby creating secondary porosity within the hollow nodules and a source of ions to support the inward growth of hollow nodule rims. Such a process could be consistent with the generally uniform size distribution of the hollow nodule voids and the subtle scaling relationship observed between hollow nodule interior void diameter and rim thickness—larger spherules (more reactant) would have been capable of supporting the formation of thicker rims.

The secondary dissolution hypothesis invokes examples from the Earth sedimentary record that offer a reasonable morphological analog to the Sheepbed hollow nodules, but neither the imaged-based observations and geochemical data presented here nor the available mineralogical data from the SAM and CheMin instruments [*Ming et al.*, 2014; *Vaniman et al.*, 2014] indicate the presence or composition of a particular precursor mineral phase within the hollow nodules. Given the lack of constraints on hollow nodule composition and possible precursor spherule mineralogy, any number of precipitation-dissolution reactions could be invoked to produce hollow nodule voids according to this hypothesis.

In a third model, hollow nodule void space represents primary porosity formed by the exsolution of gas bubbles from early diagenetic pore fluids (Figure 16b). Gas is a common constituent in sedimentary pore fluids on Earth [*Maxson*, 1940; *Cloud*, 1960; *Martens and Berner*, 1974; *Hovland et al.*, 1993; *Fleischer et al.*, 2001], and gas bubbles, often spheroidal in shape [*Reed et al.*, 2005], are known to form in muddy sediments in a wide variety of terrestrial depositional environments [*Emery*, 1945; *Shinn*, 1968; *Martens and Berner*, 1974; *Sills and Gonzalez*, 2001;

Reed et al., 2005; *Boudreau et al.*, 2005]. While most interstitial gas in pore fluids on Earth is formed during the decomposition of organic matter, there are several abiotic processes that could produce gas in sedimentary pore fluids on Mars [*Grotzinger et al.*, 2014]. Extreme changes in either temperature or pressure could cause the exsolution of dissolved atmospheric gases, such as CO_2, from pore fluids. Alternatively, the alteration of forsteritic olivine to saponitic smectite clay that occurred in the Sheepbed mudstone during early diagenesis [*Vaniman et al.,* 2014] could have provided a source of gas (H_2) to form the bubbles and clay minerals to increase the strength of the sediment and aid in the potential retention of gas-induced pore space.

Although available rover data do not permit a conclusive determination of the most likely gas composition, its source, or the precipitation reactions that might have led to hollow nodule rim formation, the gas bubble hypothesis is consistent with several of the observations presented here. First, the observed scaling relationship between rim thickness and hollow interior diameter (Figure 5), although not particularly strong, supports a model in which larger bubbles are capable of changing the pore fluid chemistry in a larger volume surrounding the bubble, thereby resulting in the precipitation of thicker rims. This scenario is consistent with the model of *van Kessel and van Kesteren* [2002] in which bubbles grow by diffusion of dissolved gas toward the bubble, such that larger bubbles have a greater region of influence than do smaller bubbles. The gas bubble hypothesis may also offer an explanation for the antithetical spatial relationship observed between nodules (particularly hollow/filled nodules) and raised ridge networks observed in the John Klein and Raised Ridges and Nodules mosaics (Figures 7 and 10). In high-strength substrates, such as a those containing a significant proportion of clay minerals, bubbles tend to remain confined by the surrounding substrate until relatively high gas pressures are reached that exceed substrate strength. Failure of the substrate results in migration of the gas bubble and crack formation [*Pollock et al.*, 2006]. Therefore, variations in substrate strength or institial gas pressure within Sheepbed sediments could explain the formation of hollow nodules (stationary gas bubbles) in portions of the Sheepbed exclusive of raised ridges (cracks) (i.e., Siebach et al., in review).

The effects of compaction and bioturbation often destroy gas-related structures prior to sediment lithification on Earth, but early diagenetic cementation can preserve these features. Birdseye structures, or sedimentary fenestrae, are common features in shallow marine sedimentary rocks on Earth and reflect early cementation of primary void space produced by gas bubbles. Fenestrae typically range from 1 to 3 mm [*Shinn*, 1968], consistent with the size range of Sheepbed hollow nodules, yet often show a substantially wider range of shapes likely associated with differential cohesive strength of organic-rich substrates. Spheroidal bubble-like features are also part of a continuum of early diagenetic, presumably gas-related [*Furniss et al.*, 1998; *Marshall and Anglin*, 2004; *Pollock et al.*, 2006] void morphologies collectively known as "molar-tooth structures" found in Precambrian shales [*Bishop and Sumner*, 2006; *Gilleaudeau and Kah*, 2010] and carbonate mudstones [*Bauerman*, 1885; *Smith*, 1968; *O'Connor*, 1972]. Neither birdseye structures nor molar-tooth structures are direct morphological or compositional analogs for the hollow nodules observed in the Sheepbed member, but these features from the Earth sedimentary record offer known examples of interstitial gas bubbles preservation in sediments during early diagenesis.

6.6. Timing of Concretion Formation

The co-occurrence of solid nodules and hollow nodules throughout the Sheepbed outcrop suggests that both nodule types formed contemporaneously, and the spherical shape of the nodules points toward an early diagenetic origin prior to compaction. If hollow nodules represent concretionary growths around primary gas bubble void space, the nodules must have formed during a phase of very early diagenesis prior to lithification of the Sheepbed mudstone. In order for gas bubbles to form and grow in the Sheepbed by displacement of sedimentary grains, these sediments would have been largely uncompacted and unlithified at the time of hollow nodule formation. The gas bubble hypothesis for hollow nodule formation, coupled with Siebach et al.'s (in review) interpretation of the raised ridges as early diagenetic subaqueous shrinkage cracks implies contemporaneous formation of both nodules (solid and hollow) and raised ridges prior to Sheepdbed lithification.

If hollow nodules represent the dissolution of a more soluble interior phase, the age constraints on solid and hollow nodules are slightly relaxed. In this scenario, the nodules need not have formed contemporaneously with the raised ridges prior to Sheepbed lithification, although the nodules must still have formed before (1) the percolation of diagenetic fluids that removed the interior cores of the hollow nodules, (2) the phase of fracturing that affected the entire Yellowknife Bay formation sequence [*Grotzinger et al.,* 2014], and (3) the diagenetic event that precipitated Ca-sulfate in veins formed during fracturing and in hollow nodule interiors

to form filled nodules [*Grotzinger et al.,* 2014; *McLennan et al.,* 2014]. Accordingly, a relatively early diagenetic interpretation is favored for the nodules in the dissolution scenario as well.

6.7. Nodules on Mars: Gale Crater Versus Meridiani Planum

Solid nodules, reminiscent of the Sheepbed nodules, have also been observed on Mars at Meridiani Planum, the field site of the MER Opportunity rover. Since landing in 2004, the Opportunity team has observed two types of nodules: hematite-rich nodules lacking internal structure, or "blueberries," recognized first in the sulfate-rich sandstones of the Burns formation at Eagle crater, Endurance crater, and Victoria crater [*Chan et al.,* 2004, 2005; *Squyres et al.*, 2004; *McLennan et al.*, 2005; *Calvin et al.*, 2008], and "newberries," small nodules observed in the Whitewater Lake rock type, a fine sandstone in the Endeavor crater rim interpreted as Noachian crust older than the sulfate-rich Burns formation [*Arvidson et al.*, 2014]. Hematite spherules were interpreted as concretions that formed during diagenesis by recharge of an active groundwater system [*Chan et al.*, 2004, 2005; *McLennan et al.*, 2005], while "newberries" have been interpreted as either impact accretionary lapilli or diagenetic concretions [*Arvidson et al.*, 2014]. In addition, features described as "hollowed spherules" have been identified at several locations in Meridiani in association with both hematite spherules and "newberries" [*Fairén et al.*, 2014], although their origin is unknown.

According to the size measurements made here, Sheepbed solid nodules (mean diameter = 0.80 mm) are generally smaller than the hematite spherules observed at Meridiani Planum (mean diameter = 3.6 mm) [*Calvin et al.*, 2008] and the "newberries" observed in Endeavor crater (typical diameters between 2 and 3 mm) [*Arvidson et al.,* 2014]. Sheepbed solid nodules are most similar in size to "mini"-spherules at Eagle crater [*Calvin et al.*, 2008], which average only 0.795 mm in diameter. One similarity between the Sheepbed solid nodules and the Meridiani "newberries" is that both features show only subtle compositional differences compared to surrounding host rock. Both Sheepbed solid nodules and "newberries" show a slight enrichment in iron, raising the possibility that the "newberries," if they are concretions, may be cemented by a similar mineral or contain similar proportions of cement. This is in contrast to the hematite spherules, which exhibit a highly distinctive Fe-enrichment compared to the host rock. Compositional and morphological differences between the Sheepbed solid nodules, hematite spherules, and "newberries" are not unexpected given the wide variation of diagenetic concretions known to exist on Earth [*Seilacher*, 2001]. What is perhaps more intriguing is that diagenetic concretions have been interpreted at three of the four major terrains (Meridiani Burns formation, Endeavor crater, and Yellowknife Bay formation of Gale crater) on the surface of Mars that have been explored by rover teams. Diagenetic concretions were not observed with the Spirit rover at Columbia Hills. Although this data set is small, the occurrence of diagenetic concretions at Meridiani Planum and Gale crater suggests that diagenetic aqueous alteration is not unusual in Martian sedimentary environments. However, diagenetic concretions are not ubiquitous in sedimentary deposits on Mars, as illustrated by their absence in other members of the Yellowknife Bay formation [*Grotzinger et al.*, 2014], and at Home Plate at Gusev crater [*Squyres et al.*, 2007]. The formation of concretions therefore requires a special set of conditions (permeable sediments, active groundwater system, saturated to supersaturated pore-fluids) not met in all sedimentary deposits on Mars, but also not rare—and possibly more common than on Earth.

In addition to the general conditions conducive to concretion formation listed above, the formation of hollow nodules like those in the Sheepbed member likely requires an even more specific set of conditions. If hollow nodules represent cemented gas bubbles, their formation requires gas-charged sediments cohesive enough to retain gas bubbles and early fluid flow through the sediments prior to compaction and lithification. The absence of hollow nodules in any of the sandstones in Yellowknife Bay may suggest that the increased cohesion of a clay-rich mudstone, like that of the Sheepbed member, may be necessary to retain gas bubbles prior to early lithification. If hollow nodules represent dissolution of a more soluble phase, specific geochemical and redox conditions must be met during diagenesis. It is possible that the conditions necessary to form hollow nodules occurred in other Martian deposits, but the specific sediment properties, composition, and timing required to form hollow nodules may not be particularly common.

6.8. Concretions and the Preservation of Martian Organics

Permeability is one of the most important factors controlling the preservation of organic matter in sediments as permeability determines how easily oxidizing diagenetic fluids can interact with and destroy reducing compounds. Just as the low permeability of shales and cherts on Earth creates conditions conducive to

organic matter preservation [*Sumner*, 2004], the decrease of permeability due to the precipitation of early diagenetic concretionary cements has the potential to protect and preserve organic material. Evidence for this in sedimentary rocks on Earth can be observed in the long-term preferential preservation of organic compounds and paleoecological indicators in early diagenetic concretions compared to the surrounding host rocks [e.g., *Maples,* 1986; *Martill,* 1990; *Orr et al.,* 2000; *Raiswell and Fisher,* 2000; *Weber et al.,* 2012]. Although organics preserved in early diagenetic concretions on Earth are typically biological in origin, this need not be the case on Mars where an abiotic origin for organic matter must be ruled out before a biological one is considered. Regardless of the origin of organic matter that may be present on Mars, early diagenetic concretions in Martian sediments have the potential to create a "taphonomic window" in which reduced compounds (e.g., organic molecules) can be preserved in otherwise oxidizing diagenetic environments. The potential for early diagenetic concretions to preserve organic material suggests that these features are among the most desirable targets in the search for organics on Mars, particularly in sediments containing reduced mineral species. Although organics have not been definitively identified in the Sheepbed mudstone [*Ming et al.,* 2014], the favorable mineralogy (clays) and the abundance of early diagenetic concretions in the Sheepbed mudstone indicates that this statigraphic interval represents the best candidate for the preservation of organic matter explored to-date by rover missions on Mars.

7. Conclusions

1. Three types of nodules are identified in the Sheepbed member in decreasing abundance: solid nodules, hollow nodules, and filled nodules.
2. Measurements of nodule aspect ratio show that all nodule types are generally spheroidal in shape.
3. Solid nodules range in size between 0.2 and 4.11 mm, average 0.80 mm in diameter, and exhibit a lognormal size distribution. Hollow nodules range in size between 0.29 and 5.40 mm, average 1.35 mm in diameter, and exhibit a normal size distribution. Average hollow nodule interior void diameter is 0.86 mm and average hollow nodule rim thickness is 0.25 mm. Filled nodules range in size between 1.18 and 5.15 mm, average 2.75 mm in diameter, and exhibit a normal size distribution.
4. Size and shape measurements suggest that hollow and filled nodules represent one population that is statistically distinct from solid nodules. This is consistent with the interpretation of *Grotzinger et al.* [2014] that filled nodules are a variant of hollow nodules that have been filled by a later phase of sulfate mineralization.
5. Solid, hollow, and filled nodules coexist in outcrop throughout the Sheepbed, although the nodule types sometimes exhibit distinct distributions. Hollow nodules, in particular, exhibit an antithetical spatial relationship raised ridges, with spindle-shaped mineralized cracks.
6. Both solid nodules and hollow/filled nodules occur in a clustered, rather than random or dispersed, pattern laterally and vertically within the Sheepbed outcrop.
7. APXS analyses indicate the presence of an Fe-bearing cement within the nodules, but ChemCam measurements suggest that the difference between nodule and host rock compositions is extremely subtle.
8. Based on the size, shape, distribution, and composition of the Sheepbed nodules, all nodule types are interpreted to be concretions formed during the early aqueous alteration of the Sheepbed mudstone by diagenetic pore fluids.
9. Hollow nodules may represent either the dissolution of a more soluble interior phase within some concretions, or concretionary growth around primary void space caused by gas bubbles trapped in the cohesive but unlithified clay-rich Sheepbed sediments.
10. Active groundwater systems may often be involved in the diagenesis of sedimentary sequences on Mars, explaining the occurrence of concretions in multiple Martian sedimentary sequences on Mars, but the specific conditions and timing of events necessary for hollow nodule formation may be less common.
11. Sediments containing nodules and hollow nodules are good candidates for the possible preservation of organic material because diagenetic concretions can create a favorable taphonomic window.

Notation

A	area (mm^2)
AR	aspect ratio
C	areal concentration (%)

d	mean feature diameter (*mm*)
n	number of features on a surface
σ	standard deviation
p	significance probability
μ	mean

Acknowledgments
We would like to thank the scientists and engineers of the MSL team, especially the MAHLI, Mastcam, ChemCam, and APXS payload uplink and downlink leads. We also thank M. Chan and D. Loope for constructive comments that helped to improve this manuscript. All data used in this paper can be obtained by contacting the corresponding author.

References

Anderson, R. C., et al. (2012), Collecting samples in Gale crater, Mars: An overview of the Mars science laboratory sample acquisition, sample processing and handling system, *Space Sci. Rev.*, *170*(1–4), 57–75, doi:10.1007/s11214-012-9898-9.

Arvidson, R. E., et al. (2014), Ancient aqueous environments at Endeavour crater, Mars, *Science*, *343*, doi:10.1126/science.1248097.

Bauerman, H. (1885), Report on the geology of the country near the forty-ninth parallel of north latitude west of the Rocky Mountains, from observations made 1859–61, *Can. Geol. Surv. Rep. Prog.*, *1882-4*, 1–41.

Bishop, J. W., and D. Y. Sumner (2006), Molar tooth structures of the Neoarchean Monteville Formation, Transvaal Supergroup, South Africa. I: Constraints on microcrystalline CaCO3 precipitation, *Sedimentology*, *53*(5), 1049–1068, doi:10.1111/j.1365-3091.2006.00801.x.

Bjørkum, P. A., and O. Walderhaug (1990), Geometrical arrangement of calcite cementation within shallow marine sandstones, *Earth Sci. Rev.*, *29*(1–4), 145–161, doi:10.1016/0012-8252(0)90033-R.

Blatt, H., G. Middleton, and R. Murray (1972), *Origin of Sedimentary Rocks*, 634 pp., Prentice-Hall, Englewood Cliffs, N. J.

Boudreau, B. P., et al. (2005), Bubble growth and rise in soft sediments, *Geology*, *33*(6), 517–520, doi:10.1130/G21259.1.

Calvin, W. M., et al. (2008), Hematite spherules at Meridiani: Results from MI, Mini-TES, and Pancam, *J. Geophys. Res.*, *113*, E12S37, doi:10.1029/2007JE003048.

Chan, M. A., B. Beitler, W. T. Parry, J. Ormö, and G. Komatsu (2004), A possible terrestrial analogue for hematite concretions on Mars, *Nature*, *429*, 731–734, doi:10.1038/nature02600.

Chan, M. A., B. Beitler Bowen, W. T. Parry, J. Ormö, and G. Komatsu (2005), Red rock and red planet diagenesis: Comparisons of Earth and Mars concretions, *GSA Today*, *15*(8), 4–10, doi:10.1130/1052-5173(2005)015[4:RRARPD]2.0.CO;2.

Chan, M. A., S. L. Potter, B. B. Bowen, W.T. Parry, L. M. Barge, W. Seiler, E. U. Petersen, and J. R. Bowman (2012), Characteristics of terrestrial ferric oxide concretions and implications for Mars, in *Sedimentary Geology of Mars*, *SEPM Spec. Publ., No. 102*, edited by J. P. Grotzinger and R. E. Milliken, pp. 253–270, SEPM, Tulsa, Okla., doi:10.2110/pec.12.102.0253.

Cloud, P. A. (1960), Gas as a sedimentary and diagenetic agent, *Am. J. Sci.* (Bradley vol.), *258-A*, 35–45.

Criss, R. E., G. A. Cooke, and S. D. Day (1988), *An Organic Origin for the Carbonate Concretions of the Ohio Shale*, *U.S. Geol. Surv. Bull., 1836*, 21 pp., U.S. Government Printing Office, Denver, Colo.

Dana, J. D. (1863), *Manual of Geology*, Bliss & Co., Philadelphia, Pa.

Deegan, C. E. (1971), The mode of origin of some late diagenetic sandstone concretions from the Scottish Carboniferous, *Scott. J. Geol.*, *7*(4), 357–365, doi:10.1144/sjg07040357.

Dix, G. R., and H. T. Mullins (1987), Shallow, subsurface growth and burial alteration of Middle Devonian calcite concretions, *J. Sed. Petr.*, *57*(1), 140–152, doi:10.1306/212F8ACB-2B24-11D7-8648000102C1865D.

Edgett, K., et al. (2012), Curiosity's Mars Hand Lens Imager (MAHLI) investigation, *Space Sci. Rev.*, *170*(1–4), 259–317, doi:10.1007/s11214-012-9910-4.

Emery, K. O. (1945), Entrapment of Air in Beach Sand, *J. Sed. Petr.*, *15*(2), 39–49.

Fairén, A., S. W. Squyres, J. P. Grotzinger, W. M. Calvin, S. W. Ruff, and the MER Athena Science Team (2014), Hollowed spherules identified with the MER Opportunity near and at Cape York, western rim of Endeavor crater, Mars, paper presented at the 45th Lunar and Planetary Science Conference, The Woodland, Tex.

Fleischer, P., T. Orsi, M. Richardson, and A. Anderson (2001), Distribution of free gas in marine sediments: A global overview, *Geo Mar. Lett.*, *21*(2), 103–122, doi:10.1007/s003670100072.

Fralick, P., J. Grotzinger, and L. Edgar (2012), Potential recognition of accretionary lapilli in distal impact deposits on Mars, in *Sedimentary Geology of Mars*, edited by J. P. Grotzinger and R. E. Milliken, pp. 211–227, The Society of Economic Paleontologists and Mineralogists, Tulsa, Okla., doi:10.2110/pec.12.102.0211.

Furniss, G., J. F. Rittel, and D. Winston (1998), Gas bubble and expansion crack origin of "molar-tooth" calcite structures in the middle Proterozoic Belt Supergroup, western Montana, *J. Sediment. Res.*, *68*(1), 104–114, doi:10.2110/jsr.68.104.

Galimov, E. M., and Y. P. Girin (1968), Variation in isotopic composition of carbon in the process of formation of carbonate concretions, *Geochem. Int.*, *5*(1), 178–182.

Gilleaudeau, G. J., and L. C. Kah (2010), Molar-tooth crack formation and the Proterozoic marine substrate: Insights from the Belt Supergroup, Montana and the Atar Group, Mauritania, GSA Annual Meeting, Paper No. 51-7.

Gluyas, J. G. (1984), Early carbonate diagenesis within Phanerozoic shales and sandstones of the NW European shelf, *Clay Miner.*, *19*(3), 309–321.

Grant, J. A., S. A. Wilson, N. Mangold, F. Calef III, and J. P. Grotzinger (2014), The timing of alluvial activity in Gale crater, Mars, *Geophys. Res. Lett.*, *41*, 1142–1148, doi:10.1002/2013GL058909.

Grotzinger, J. P., et al. (2014), A habitable fluvio-lacustrine environment at Yellowknife Bay, Gale crater, Mars, *Science*, *343*(6169), doi:10.1126/science.1242777.

Hovland, M., et al. (1993), The global flux of methane from shallow submarine sediments, *Chemosphere*, *26*, 559–578, doi:10.1016/0045-6535(93)90442-8.

Hudson, J. D., and J. E. Andrews (1987), The diagenesis of the Great Estuarine Group, Middle Jurassic, Inner Hebrides, Scotland, *Geol. Soc. London Spec. Publ.*, *36*(1), 259–276, doi:10.1144/gsl.sp.1987.036.01.19.

Kettler, R. M., D. B. Loope, and K. A. Weber (2011), Follow the water: Connecting a CO_2 reservoir and bleacher sandstone to iron-rich concretions in the Navajo Sandstone of south-central Utah, REPLY to COMMENT, *Geology*, *39*(11), E251–E252, doi:10.1130/G32550Y.1.

Knoke, R. (1966), Untersuchungen zur Diagenese und Kalkkonkretionen un umgebenden Tonschiefern, *Contrib. Mineral. Petrol.*, *12*, 139–167.

Loope, D., R. M. Kettler, K. A. Weber, N. L. Hinrichs, and D. T. Burgess (2012), Rinded iron-oxide concretions: Hallmarks of altered siderite masses of both early and late diagenetic origin, *Sedimentology*, *59*, 1769–1781, doi:10.1111/j.1365-3091.2012.01325.x.

Maples, C. G. (1986), Enhanced paleoecological and paleoenvironmental interpretations result from analysis of early diagenetic concretions in Pennsylvanian shales, *PALAIOS*, *1*(5), 512–516, doi:10.2307/3514633.

Marshall, D., and C. D. Anglin (2004), CO2-clathrate destabilization: A new model of formation for molar tooth structures, *Precambrian Res.*, *129*(3–4), 325–341, doi:10.1016/j.precamres.2003.10.007.

Martens, C. S., and R. A. Berner (1974), Methane production in the interstitial waters of sulfate-depleted marine sediments, *Science*, *185*(4157), 1167–1169, doi:10.1126/science.185.4157.1167.
Martill, D. M. (1990), Macromolecular resolution of fossilized muscle tissue from an elopomorph fish, *Nature*, *346*(6280), 171–172.
Maxson, J. H. (1940), Gas pits in non-marine sediments, *J. Sediment. Res.*, *10*(3), 142–145, doi:10.1306/d42690bc-2b26-11d7-8648000102c1865d.
McBride, E. F., M. D. Picard, and R. L. Folk (1994), Oriented concretions, Ionian Coast, Italy: Evidence of groundwater flow direction, *J. Sediment. Res.*, *64*(3a), 535–540, doi:10.1306/d4267dfc-2b26-11d7-8648000102c1865d.
McBride, A. Abdel-Wahab, and A. R. M. El-Younsy (1999), Origin of spheroidal chert nodules, Drunka Formation (Lower Eocene), Egypt, *Sedimentology*, *46*(4), 733–755, doi:10.1046/j.1365-3091.1999.00253.x.
McLennan, S. M., et al. (2005), Provenance and diagenesis of the evaporite-bearing Burns formation, Meridiani Planum, Mars, *Earth Planet. Sci. Lett.*, *240*(1), 95–121, doi:10.1016/j.epsl.2005.09.041.
McLennan, S. M., et al. (2014), Elemental geochemistry of sedimentary rocks at Yellowknife Bay, Gale crater, Mars, *Science*, *343*(6169), doi:10.1126/science.1244734.
Ming, D. W., et al. (2014), Volatile and organic compositions of sedimentary rocks in Yellowknife Bay, Gale crater, Mars, *Science*, *343*(6169), doi:10.1126/science.1245267.
Minitti, M. E., et al. (2013), MAHLI at the Rocknest sand shadow: Science and science-enabling activities, *J. Geophys. Res. Planets*, *118*, 2338–2360, doi:10.1002/2013JE004426.
Mozley, P. S. (1996), The internal structure of carbonate concretions in mudrocks: A critical evaluation of the conventional concentric model of concretion growth, *Sediment. Geol.*, *103*(1–2), 85–91, doi:10.1016/0037-0738(95)00087-9.
Mozley, P. S., and J. M. Davis (2005), Internal structure and mode of growth of elongate calcite concretions: Evidence for small-scale, microbially induced, chemical heterogeneity in groundwater, *Geol. Soc. Am. Bull.*, *117*(11–12), 1400–1412, doi:10.1130/b25618.1.
Newberry, J. S. (1873), *Geology and Palaeontology, Part II. Palaeontology*, Rep. of the Geological Survey of Ohio, vol. 1, Nevins & Myers, Columbus, Ohio.
O'Connor, M. P. (1972), Classification and environmental interpretation of the cryptalgal organosedimentary "molar-tooth" structure from the late Precambrian Belt-Purcell Supergroup, *J. Geol.*, *80*(5), 592–610, doi:10.1086/627783.
Orr, P. J., D. E. G. Briggs, D. J. Siveter, and D. J. Siveter (2000), Three-dimensional preservation of a non-biomineralized arthropod in concretions in Silurian volcaniclastic rocks from Herefordshire, England, *J. Geol. Soc.*, *157*(1), 173–186, doi:10.1144/jgs.157.1.173.
Pollock, M. D., L. C. Kah, and J. K. Bartley (2006), Morphology of molar-tooth structures in Precambrian carbonates: Influence of substrate rheology and implications for genesis, *J. Sediment. Res.*, *76*(2), 310–323, doi:10.2110/jsr.2006.021.
Potter, S. L., M. A. Chan, E. U. Petersen, M. D. Dyar, and E. Sklute (2011), Characterization of Navajo Sandstone concretions: Mars comparison and criteria for distinguishing diagenetic origins, *Earth Planet. Sci. Lett.*, *301*, 444–456, doi:10.1016/j.epsl.2010.11.027.
Raiswell, R. (1971), The growth of Cambrian and Liassic concretions, *Sedimentology*, *17*(3-4), 147–171, doi:10.1111/j.1365-3091.1971.tb01773.x.
Raiswell, R. (1988), Evidence for surface reaction-controlled growth of carbonate concretions in shales, *Sedimentology*, *35*(4), 571–575, doi:10.1111/j.1365-3091.1988.tb01236.x.
Raiswell, R., and N. J. M. White (1978), Spatial Aspects of Concretionary Growth in the Upper Lias of Northeast England, Sedimentary Geology, *20*, 291–300, doi:10.1016/0037-0738(78)90059-3.
Raiswell, R., and Q. J. Fisher (2000), Mudrock-hosted carbonate concretions: A review of growth mechanisms and their influence on chemical and isotopic composition, *J. Geol. Soc.*, *157*(1), 239–251, doi:10.1144/jgs.157.1.239.
Reed, A. H., B. P. Boudreau, C. Algar, and Y. Furukawa (2005), Morphology of gas bubbles in mud: A microcomputed tomographic evaluation, Proceedings of the International Conference "Underwater Acoustic Measurements: Technologies & Results", Herklion, Crete, Greece, 28th June–1st July.
Schultz, C. B. (1941), The pipy concretions of the Arikaree, *Bull. Univ. Nebr. State Mus.*, *2*(8), 69–81.
Seilacher, A. (2001), Concretion morphologies reflecting diagenetic and epigenetic pathways, *Sediment. Geol.*, *143*(1–2), 41–57, doi:10.1016/S0037-0738(01)00092-6.
Shinn, E. A. (1968), Practical significance of birdseye structures in carbonate rocks, *J. Sediment. Res.*, *38*(1), 215–223, doi:10.1306/74d7191f-2b21-11d7-8648000102c1865d.
Sills, G. C., and R. Gonzalez (2001), Consolidation of naturally gassy soft soil, *Geotechnique*, *51*(7), 629–639, doi:10.1680/geot.2001.51.7.629.
Simonson, B. M. (2003), Petrographic criteria for recognizing certain types of impact spherules in well-preserved Precambrian successions, *Astrobiology*, *3*(1), 49–65, doi:10.1089/153110703321632417.
Simonson, B. M., and B. P. Glass (2004), Spherule layers—Records of ancient impacts, *Annu. Rev. Earth Planet. Sci.*, *32*(1), 329–361, doi:10.1146/annurev.earth.32.101802.120458.
Smith, A. G. (1968), The origin and deformation of some "molar-tooth" structures in the Precambrian Belt–Purcell Supergroup, *J. Geol.*, *76*(4), 426–443, doi:10.1086/627341.
Sorby, H. C. (1908), On the application of quantitative methods to the study of the structure and history of rocks, *Q. J. Geol. Soc.*, *64*(1–4), 171–233, doi:10.1144/gsl.jgs.1908.064.01-04.12.
Squyres, S. W., et al. (2004), The Opportunity Rover's Athena Science Investigation at Meridiani Planum, Mars, *Science*, *306*(5702), 1698–1703, doi:10.1126/science.1106171.
Squyres, S. W., et al. (2007), Pyroclastic activity at home plate in Gusev crater, Mars, *Science*, *316*(5825), 738–742, doi:10.1126/science.1139045.
Sumner, D. Y. (2004), Poor preservation potential of organics in Meridiani Planum hematite-bearing sedimentary rocks, *J. Geophys. Res.*, *109*, E12007, doi:10.1029/2004JE002321.
Tomkieff, S. (1927), On the occurrence and mode of origin of certain kaolinite-bearing nodules in the coal measures, *Proc. Geol. Assoc.*, *38*(4), 518–547, IN8, doi:10.1016/S0016-7878(27)80017-9.
van der Burg, W. J. (1969), The formation of rattle stones and the climatological factors which limited their distribution in the Dutch Pleistocene. 1. The formation of rattle stones, *Palaeogeogr. Palaeoclimatol. Palaeoecol.*, *6*, 105–124, doi:10.1016/0031-0182(69)90007-8.
van der Burg, W. J. (1970), The formation of rattle stones and the climatological factors which limited their distribution in the Dutch Pleistocene. 2. The climatological factors, *Palaeogeogr. Palaeoclimatol. Palaeoecol.*, *7*, 297–308, doi:10.1016/0031-0182(70)90098-2.
van Kessel, T., and W. G. van Kesteren (2002), Gas production and transport in artificial sludge depots, *Waste Manage.*, *22*(1), 19–28.
Vaniman, D. T., et al. (2014), Mineralogy of a mudstone at Yellowknife Bay, Gale crater, Mars, *Science*, *343*(6169), doi:10.1126/science.1243480.
Weber, K., T. L. Spanbauer, D. Wacey, M. R. Kilburn, D. B. Loope, and R. M. Kettler (2012), Biosignatures link microorganisms to iron mineralization in a paleoaquifer, *Geology*, *40*, 747–750, doi:10.1130/G33062.1.
Wiens, R. C., et al. (2012), The ChemCam instrument suite on the Mars Science Laboratory (MSL) rover: Body unit and combined system tests, *Space Sci. Rev.*, *170*(1–4), 167–227, doi:10.1007/s11214-012-9902-4.
Wiens, R. C., et al. (2013), Pre-flight calibration and initial data processing for the ChemCam laser-induced breakdown spectroscopy (LIBS) instrument on the Mars Science Laboratory rover, *Spectrochim. Acta, Part B*, *82*, 1–27, doi:10.1016/j.sab.2013.02.003.